



**HAL**  
open science

## Control of Ca<sup>2+</sup> signals by astrocyte nanoscale morphology at tripartite synapses

Audrey Denizot, Misa Arizono, Valentin Nägerl, Hugues Berry, Erik de Schutter

### ► To cite this version:

Audrey Denizot, Misa Arizono, Valentin Nägerl, Hugues Berry, Erik de Schutter. Control of Ca<sup>2+</sup> signals by astrocyte nanoscale morphology at tripartite synapses. *Glia*, 2022, 10.1002/glia.24258. hal-03582629v1

**HAL Id: hal-03582629**

**<https://inria.hal.science/hal-03582629v1>**

Submitted on 21 Feb 2022 (v1), last revised 12 Oct 2022 (v2)

**HAL** is a multi-disciplinary open access archive for the deposit and dissemination of scientific research documents, whether they are published or not. The documents may come from teaching and research institutions in France or abroad, or from public or private research centers.

L'archive ouverte pluridisciplinaire **HAL**, est destinée au dépôt et à la diffusion de documents scientifiques de niveau recherche, publiés ou non, émanant des établissements d'enseignement et de recherche français ou étrangers, des laboratoires publics ou privés.

# Control of $\text{Ca}^{2+}$ signals by astrocyte nanoscale morphology at tripartite synapses

Audrey Denizot<sup>1\*</sup>, Misa Arizono<sup>2,3</sup>, U. Valentin Nägerl<sup>2,3</sup>, Hugues Berry<sup>4,5</sup>, Erik De Schutter<sup>1</sup>

\*For correspondence:  
[audrey.denizot3@oist.jp](mailto:audrey.denizot3@oist.jp) (AD)

<sup>1</sup>Okinawa Institute of Science and Technology, Computational Neuroscience Unit, Onna-Son, Japan; <sup>2</sup>Interdisciplinary Institute for Neuroscience, Université de Bordeaux, Bordeaux, France; <sup>3</sup>Interdisciplinary Institute for Neuroscience, CNRS UMR 5297, Bordeaux, France; <sup>4</sup>Univ Lyon, LIRIS, UMR5205 CNRS, F-69621, Villeurbanne, France; <sup>5</sup>INRIA, F-69603, Villeurbanne, France

**Abstract** Astrocytic  $\text{Ca}^{2+}$  signals regulate synaptic activity. Most of those signals are spatially restricted to microdomains and occur in fine processes that cannot be resolved by diffraction-limited light microscopy, restricting our understanding of their physiology. Those fine processes are characterized by an elaborate morphology, forming the so-called spongiform domain, which could, similarly to dendritic spines, shape local  $\text{Ca}^{2+}$  dynamics. Because of the technical limitations to access the small spatial scale involved, the effect of astrocyte morphology on  $\text{Ca}^{2+}$  microdomain activity remains poorly understood. Here, we use computational tools and realistic 3D geometries of fine processes based on recent super-resolution microscopy data to investigate the mechanistic link between astrocytic nanoscale morphology and local  $\text{Ca}^{2+}$  activity. Simulations demonstrate that the nano-morphology of astrocytic processes powerfully shapes the spatio-temporal properties of  $\text{Ca}^{2+}$  signals and promotes local  $\text{Ca}^{2+}$  activity. The model predicts that this effect is attenuated upon astrocytic swelling, hallmark of brain diseases, which we confirm experimentally in hypo-osmotic conditions. Upon repeated neurotransmitter release events, the model predicts that swelling hinders astrocytic signal propagation. Overall, this study highlights the influence of the complex morphology of astrocytes at the nanoscale and its remodeling in pathological conditions on neuron-astrocyte communication at tripartite synapses.

## Introduction

Astrocytes are glial cells of the central nervous system that are essential for brain development and function, playing key roles in e.g ion homeostasis, neurotransmitters uptake and lactate metabolism (see (*Verkhratsky and Nedergaard, 2018*) for more details). Furthermore, astrocytes can modulate neuronal communication at synapses. In response to the release of neurotransmitters from neurons,  $\text{Ca}^{2+}$  signals are observed in astrocytes, which can trigger the release of neuroactive molecules by the astrocyte, gliotransmitters. The first type of astrocytic  $\text{Ca}^{2+}$  signals that has been observed was  $\text{Ca}^{2+}$  waves that propagate through gap junctions in astrocyte networks (*Giaume and Venance, 1998*).  $\text{Ca}^{2+}$  waves are also observed within the branches of single astrocytes, sporadically propagating to the soma (*Haustein et al., 2014; Bindocci et al., 2017*). The recent development of  $\text{Ca}^{2+}$  imaging techniques that provide better spatial and temporal resolution has revealed the existence of spatially-restricted  $\text{Ca}^{2+}$  signals in astrocytes, referred to as microdomains

41 or hotspots (*Di Castro et al., 2011; Panatier et al., 2011; Stobart et al., 2018a; Srinivasan et al.,*  
42 *2015; Shigetomi et al., 2013; Sherwood et al., 2017; Otsu et al., 2015; Lind et al., 2013; Bindocci*  
43 *et al., 2017; Agarwal et al., 2017; Arizono et al., 2020*). Those local  $\text{Ca}^{2+}$  signals account for as  
44 much as 80 % of astrocytic  $\text{Ca}^{2+}$  activity and occur in fine astrocytic processes, also referred to as  
45 branchlets, which occupy 75 % of the astrocytic volume (*Bindocci et al., 2017*), referred to as the  
46 spongiform domain or gliapil. Given that one astrocyte can contact tens of thousands of synapses  
47 simultaneously in the mouse hippocampus (*Bushong et al., 2002*) and up to two million in the  
48 human brain (*Oberheim et al., 2006*) through these fine processes, local, fast  $\text{Ca}^{2+}$  signals might  
49 enable the astrocyte to powerfully yet precisely control the flow of information through synaptic  
50 circuits.

51

52 Elaborate cellular morphologies lend themselves to the fine compartmentalization of signals.  
53 For example, the anatomical design of dendritic spines restricts the spread of  $\text{Ca}^{2+}$  to the acti-  
54 vated synapse, ensuring that there is little cross-talk between different synapses and that the local  
55  $\text{Ca}^{2+}$  concentration can go very high (*Santamaria et al., 2011; Tønnesen et al., 2014; Yuste et al.,*  
56 *2000; Noguchi et al., 2005; Yasuda, 2017; Holcman and Schuss, 2011*). It is thus likely that the  
57 complex organization of the reticular structure of astrocytes plays a key role in shaping local  $\text{Ca}^{2+}$   
58 microdomains (*Rusakov, 2015*). For example, the complex shape of Bergmann glia has been pro-  
59 posed to potentially restrict  $\text{Ca}^{2+}$  signals to the vicinity of synapses (*Grosche et al., 1999*). Similarly,  
60 perisynaptic enlargements called “astrocytic compartments” along major branches of astrocytes  
61 also exhibit  $\text{Ca}^{2+}$  signals (*Panatier et al., 2011*). Fine processes of the spongiform domain, however,  
62 cannot be resolved by diffraction-limited light microscopy (*Rusakov, 2015*), so that the contribution  
63 of their nanoscale morphology to shaping local  $\text{Ca}^{2+}$  signals is poorly understood. Our recent 3D  
64 super-resolution Stimulated Emission Depletion (STED) microscopy study (*Arizono et al., 2020*) re-  
65 vealed that particular shapes of the complex meshwork of astrocytic processes, reminiscent of  
66 dendritic spines, are associated with compartmentalized  $\text{Ca}^{2+}$  signals. Furthermore, aberrant  $\text{Ca}^{2+}$   
67 signals (*Shigetomi et al., 2019*) and changes in astrocytic morphology, such as “astrocytic swelling”,  
68 occur in pathological conditions such as brain injury, including ischemic, traumatic, hemorrhagic  
69 and metabolic injuries, stroke and epilepsy (*Lafrenaye and Simard, 2019*). Interestingly, our recent  
70 STED study reported that swelling can also occur at the level of fine astrocytic processes (*Arizono*  
71 *et al., 2021a*). The effect of such a remodeling of astrocytic nano-morphology on the local  $\text{Ca}^{2+}$   
72 signals involved in regulating synapses yet remains unclear. Together, there is a great interest  
73 in understanding the mechanistic link between the nano-morphology of astrocytic processes and  
74  $\text{Ca}^{2+}$  profiles in health and disease. Changing cell morphology experimentally is not straightforward  
75 and can affect cell physiology, notably when the osmolarity of the extracellular space is altered. By  
76 contrast, computational approaches can finely tune geometrical properties, resulting in more con-  
77 trolled investigations than what could be done experimentally. Computational models are thus  
78 tools of choice to investigate the isolated impact of morphological parameters on  $\text{Ca}^{2+}$  dynamics.

79 Here, we use computational tools to investigate the effect of astrocyte nanoscale morphology  
80 on local  $\text{Ca}^{2+}$  activity, in healthy and swelling conditions. To account for the stochasticity of molec-  
81 ular interactions in small volumes such as those of astrocyte processes, we use the stochastic  
82 voxel-based model of  $\text{Ca}^{2+}$  signals from Denizot et al. (*Denizot et al., 2019a*). Idealized geome-  
83 tries of branchlets were designed based on super-resolution microscopy images recently reported  
84 in live tissue (*Arizono et al., 2020*). Branchlets consist in alternations of structures referred to as  
85 nodes and shafts. At this spatial scale, swelling resulting from hypo-osmotic conditions results in  
86 an increased diameter of shafts, without altering node morphology (see Fig 3 from (*Arizono et al.,*  
87 *2021b*)). To explore how such changes in morphology affect  $\text{Ca}^{2+}$  signalling, we performed simula-  
88 tions in geometrical models of branchlets of varying shaft widths. Our simulation results suggest  
89 that astrocyte swelling results in an increased diffusion flux, which decreases  $\text{Ca}^{2+}$  peak probabil-  
90 ity, duration and amplitude in the stimulated and neighboring nodes. To test those predictions,  
91 we performed  $\text{Ca}^{2+}$  recordings in organotypic hippocampal cultures in hypo-osmotic conditions,

92 which result in increased shaft width without altering node width.  $\text{Ca}^{2+}$  activity in hypo-osmotic  
93 conditions was decreased compared to  $\text{Ca}^{2+}$  activity in healthy tissue, in line with our model pre-  
94 dictions. In case of repeated node stimulation, thin shafts allowed signal propagation even if some  
95 stimuli were omitted. Thin shafts thus allow for more robust signal propagation within the gliapil,  
96 which is hindered in swelling conditions.

97

98 Overall, this study sheds light on the influence of the nanoscale morphology of the complex  
99 spongiform domain of astrocytes on  $\text{Ca}^{2+}$  microdomain activity. Importantly, our results provide  
100 evidence that node compartmentalization, resulting from a reduced diffusion efflux from nodes  
101 connected to thin shafts, can increase  $\text{Ca}^{2+}$  activity locally. Our study indicates that pathological  
102 changes in nanoscale astrocyte morphology may substantially affect their  $\text{Ca}^{2+}$  activity.

## 103 Results

### 104 Geometrical representation of typical astrocyte processes

105 In order to investigate the effect of astrocyte nanoscale morphology on the spatio-temporal  
106 properties of  $\text{Ca}^{2+}$  signals, we have designed geometries of typical astrocyte processes, derived  
107 from the recent characterization of their ultrastructure at a high spatial resolution (50 nm in x-  
108 y) in organotypic hippocampal culture as well as in acute slices and *in vivo* (Arizono *et al.*, 2020).  
109 Geometries consist of alternations of bulbous structures, nodes, connected to each other with  
110 cylindrical structures, referred to as shafts. To reproduce the morphological changes of processes  
111 associated with cell swelling reported in hypo-osmotic conditions (Fig 3 in (Arizono *et al.*, 2021b)),  
112 geometries with different shaft width  $d_{\text{shaft}}$  and constant node width were designed (Fig 1A). In  
113 accordance with node-shaft structures observed experimentally (Arizono *et al.*, 2020), node width  
114 was set to 380 nm. To model astrocytic  $\text{Ca}^{2+}$  activity with a high spatial resolution while taking into  
115 account the randomness of reactions in small volumes, we used the stochastic voxel-based model  
116 from Denizot *et al.* (Denizot *et al.*, 2019a) (see Methods). The reactions included in the model  
117 are presented in Fig 1B and in the Methods section. As the majority of  $\text{Ca}^{2+}$  signals in astrocytes  
118 result from the opening of Inositol 3-Phosphate receptors ( $\text{IP}_3\text{Rs}$ ), located at the membrane of the  
119 endoplasmic reticulum (ER) (Srinivasan *et al.*, 2015), signals in the model result from the opening  
120 of  $\text{IP}_3\text{Rs}$  (see Denizot *et al.* (Denizot *et al.*, 2019a) for discussion on the model's assumptions and  
121 limitations).

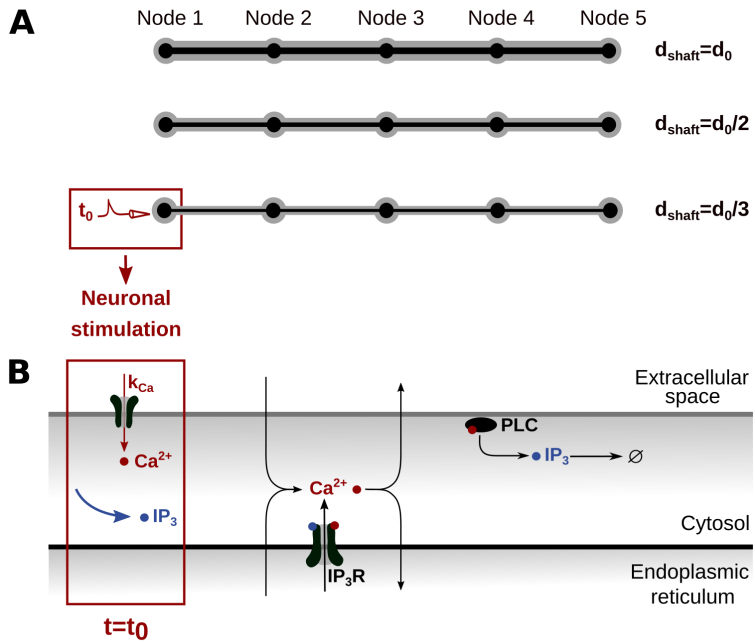


**Figure 1. Geometries and kinetic scheme used for simulating  $Ca^{2+}$  dynamics in node/shaft structures of the gliapil.** (A) Geometries reproducing node/shaft geometries of the gliapil (Arizono *et al.*, 2020; Panatier *et al.*, 2014) were designed. Nodes are approximated as spheres of diameter 380 nm and shafts as 1  $\mu\text{m}$ -long cylinders. The geometries designed in this study, referred to as “5 nodes”, contain 5 identical nodes and 4 identical shafts. Geometries were characterized by different shaft widths:  $d_{\text{shaft}} = d_0 = 380\text{nm}$ ,  $d_{\text{shaft}} = \frac{d_0}{2}$  and  $d_{\text{shaft}} = \frac{d_0}{3}$ . The associated cytosolic volume, plasma and ER membrane areas are presented in Table 1. (B) Biochemical processes included in the model.  $Ca^{2+}$  can enter/exit the cytosol from/to the extracellular space or the endoplasmic reticulum (ER), resulting from the activity of  $Ca^{2+}$  channels/pumps.  $Ca^{2+}$  and  $IP_3$  diffuse in the cytosol following Brownian motion. The kinetics of  $IP_3R$  channels corresponds to the 8-state Markov model from (Denizot *et al.*, 2019b), adapted from (De Young and Keizer, 1992; Bezprozvanny *et al.*, 1991). When both  $IP_3$  and  $Ca^{2+}$  are bound to  $IP_3R$  activating binding sites, the  $IP_3R$  is in open state and  $Ca^{2+}$  enters the cytosol.  $Ca^{2+}$  can activate Phospholipase C  $\delta$  (PLC $\delta$ ), which results in the production of  $IP_3$ . For more details, please refer to (Denizot *et al.*, 2019b). Neuronal stimulation is simulated as an infusion of  $IP_3$  in the cytosol and the opening of  $Ca^{2+}$  channels at the plasma membrane with an influx rate  $k_{Ca}$  (see Methods).

**Figure 1–Figure supplement 1.** Sensitivity study of the effect of voxel size on  $Ca^{2+}$  signals.

**Figure 1–source data 1.** Characteristics of meshes used to investigate the effect of voxel size on  $Ca^{2+}$  signals (Table Supplement 1).

## 122 Thin shafts favor node compartmentalization

123 In order to test whether the geometries designed in this study are a good approximation of  
 124 the ultrastructure of the gliapil, we have compared molecular diffusion flux in those geometries  
 125 with those reported experimentally. To do so, we simulated photobleaching experiments and com-  
 126 pared our results to experimental results from Arizono *et al.* (Arizono *et al.*, 2020). The principle  
 127 of bleaching simulations is presented in the Methods section and in Supplemental Movie 1. Here,  
 128 we refer to an increased node compartmentalization when the time to recovery after bleaching,  $\tau$ ,  
 129 increases (see Fig 2B).

130  
 131 Bleaching traces in simulations are both qualitatively (Fig 2B) and quantitatively (Fig 2C) similar  
 132 to experimental bleaching traces, for shaft width  $d_{\text{shaft}} = d_0$  and  $d_{\text{shaft}} = \frac{d_0}{2}$ . Indeed, no significant  
 133 difference of  $I_0$  (Fig 2C1),  $I_{inf}$  (Fig 2C2) and  $\tau$  (Fig 2C3) was observed between simulations and ex-  
 134 perimental traces. Simulations were also performed with  $d_{\text{shaft}} = \frac{d_0}{3}$ . Our simulations successfully  
 135 reproduce experimental bleaching experiments and suggest that  $\tau$ , and thus node compartmental-

**Table 1.** Characteristics of the geometries of astrocyte branchlets used in this study.  $V_{\text{cyt}}$  is the cytosolic volume,  $S_{\text{PM}}$  is the area of the plasma membrane and  $S_{\text{ER}}$  is the area of the ER membrane. Volumes are expressed in  $\text{nm}^3$  and areas in  $\text{nm}^2$ . Meshes are available at <http://modeldb.yale.edu/266928>, access code: lto42@tpk3D?

Geom	$V_{\text{cyt}} (\text{nm}^3)$	$S_{\text{PM}} (\text{nm}^2)$	$S_{\text{ER}} (\text{nm}^2)$
"5nodes" $d_{\text{shaft}} = d_0$	$6.20 \times 10^8$	$7.73 \times 10^6$	$2.19 \times 10^6$
"5nodes" $d_{\text{shaft}} = d_0/2$	$2.63 \times 10^8$	$4.95 \times 10^6$	$1.28 \times 10^6$
"5nodes" $d_{\text{shaft}} = d_0/3$	$1.95 \times 10^8$	$4.10 \times 10^6$	$9.99 \times 10^5$
"No ER" $d_{\text{shaft}} = d_0$	$6.73 \times 10^8$	$7.73 \times 10^6$	0.00
"No ER" $d_{\text{shaft}} = d_0/2$	$2.83 \times 10^8$	$4.95 \times 10^6$	0.00
"No ER" $d_{\text{shaft}} = d_0/3$	$2.10 \times 10^8$	$4.09 \times 10^6$	0.00
"Node ER" $d_{\text{shaft}} = d_0$	$6.67 \times 10^8$	$7.75 \times 10^6$	$4.17 \times 10^5$
"Node ER" $d_{\text{shaft}} = d_0/2$	$2.74 \times 10^8$	$4.96 \times 10^6$	$4.37 \times 10^5$
"Node ER" $d_{\text{shaft}} = d_0/3$	$2.00 \times 10^8$	$4.11 \times 10^6$	$4.41 \times 10^5$
"Cyl ER" $d_{\text{shaft}} = d_0$	$6.27 \times 10^8$	$7.74 \times 10^6$	$2.03 \times 10^6$
"Cyl ER" $d_{\text{shaft}} = d_0/2$	$2.77 \times 10^8$	$4.95 \times 10^6$	$8.78 \times 10^5$
"Cyl ER" $d_{\text{shaft}} = d_0/3$	$2.07 \times 10^8$	$4.09 \times 10^6$	$5.86 \times 10^5$

136 ization, increases when shaft width decreases (Fig 2C3). This result is not surprising as a decreased  
137 shaft width results in a smaller size of the exit point for diffusing molecules from the node. This  
138 is similar to e.g dendritic spines, which compartmentalization is increased for thinner spine necks  
139 (*Santamaria et al., 2011; Tønnesen et al., 2014*). The geometries that we have designed can thus  
140 be considered as a reasonable approximation of the ultrastructure of the gliapil observed experi-  
141 mentally in live tissue.

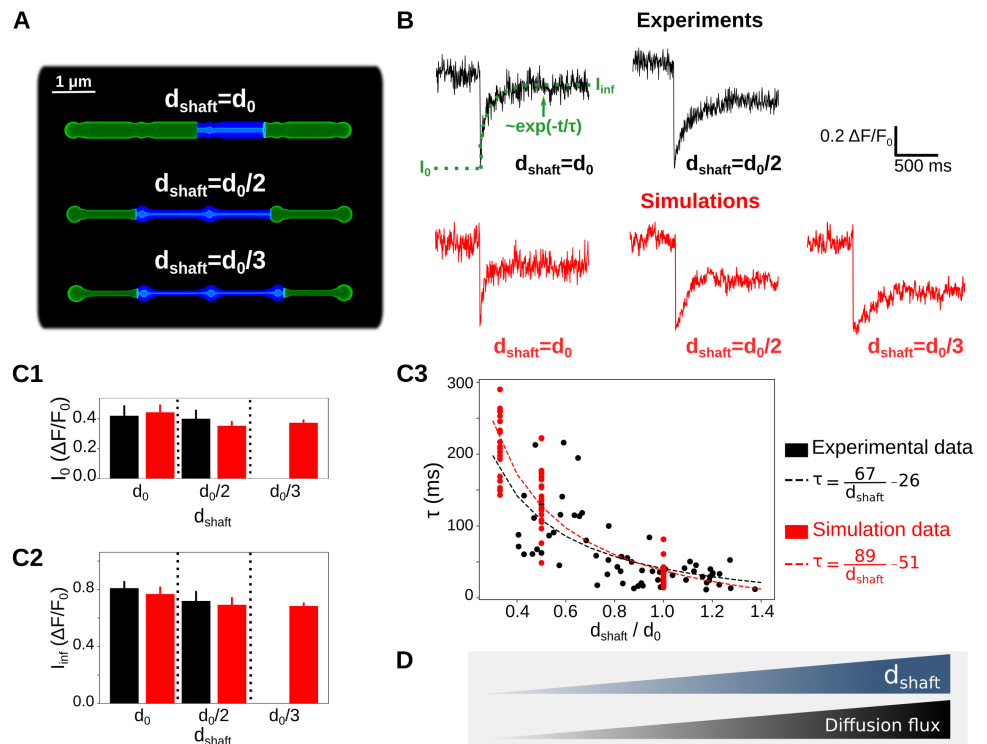


**Figure 2. Simulations confirm that thin shafts favor node compartmentalization.** (A) Geometries of different shaft widths  $d_{\text{shaft}}$ ,  $d_{\text{shaft}} = d_0$ ,  $\frac{d_0}{2}$  and  $\frac{d_0}{3}$ , used in the bleaching simulations. Blue color represents the bleached volume, which varied depending on the value of  $d_{\text{shaft}}$  in order to fit experimental values of  $I_0$  and  $I_{\text{inf}}$ . (B) Representative experimental (top) and simulation (bottom) traces for different shaft width values.  $I_0$ ,  $I_{\text{inf}}$  and  $\tau$  were calculated using Eq 1. Note that simulations were also performed for  $d_{\text{shaft}} = \frac{d_0}{3}$ . (C) Quantification of  $I_0$  (C1),  $I_{\text{inf}}$  (C2) and  $\tau$  (C3) values in simulations (red) compared to experiments (black). Note that no experimental data was available for  $d_{\text{shaft}} = \frac{d_0}{3}$ . In C1 and C2,  $n=5 \times 2$  and  $20 \times 3$  for experiments and simulations, respectively. Data are presented as mean  $\pm$  STD. In C3,  $n=66$  and  $n=20 \times 3$  for experiments and simulations, respectively.  $\tau$  is negatively correlated to  $d_{\text{shaft}}$  in experiments ( $n=66$  from 7 slices; Spearman  $r=-0.72$ ,  $p<0.001$  \*\*\*) and simulations ( $n=60$ ; Spearman  $r=-0.89$ ,  $p<0.001$  \*\*\*). Black and red lines represent curve fit of  $\tau$  as a function of  $d_{\text{shaft}}$  of the form  $\tau = a * \frac{1}{d_{\text{shaft}}} + b$  for experiments and simulations, respectively. (D) Schematic summarizing the conclusion of this figure: diffusion flux increases with  $d_{\text{shaft}}$ . In that sense, thin shafts favor node compartmentalization. Data in panels C1 and C2 are represented as mean  $\pm$  STD,  $n=20$  for each geometry.

**Figure 2-video 1.** Movie of a simulated bleaching experiment, with  $d_{\text{shaft}} = \frac{d_0}{2}$ . Fluorescing ZsGreen molecules are in red and bleached, non-fluorescing, ZsGreen are in yellow.

## 142 Thin shafts enhance $\text{Ca}^{2+}$ activity in nodes

143 80% of astrocyte  $\text{Ca}^{2+}$  activity occurs in the gliopil (*Bindocci et al., 2017*), which suggests that  
 144 most neuron-astrocyte communication occurs at fine astrocytic processes. As we observed that  
 145 a decreased shaft width is associated with a decreased diffusion flux, i.e an increased compart-  
 146 mentalization of nodes, we have tested whether this effect influences  $\text{Ca}^{2+}$  activity upon neuronal  
 147 stimulation. To do so, we have first analyzed  $\text{Ca}^{2+}$  signals resulting from a single neuronal stimula-  
 148 tion, which was simulated as an infusion of  $\text{IP}_3$  and  $\text{Ca}^{2+}$  in the stimulated node, node 1 (see Meth-  
 149 ods). Those parameters encompass the  $\text{IP}_3$  production by phospholipase C following the activation  
 150 of  $G_q$ -G-protein-coupled receptors (GPCRs) resulting from the binding of neuronal glutamate, ATP  
 151 and noradrenaline to  $G_q$  proteins and  $\text{Ca}^{2+}$  entry at the plasma membrane through  $\text{Ca}^{2+}$  channels,  
 152 ionotropic receptors or the sodium/calcium exchanger (NCX) functioning in reverse mode (*Ahmad-*  
 153 *pour et al., 2021; Semyanov et al., 2020*). Signals were recorded both in the stimulated node, node  
 154 1, and in the neighboring node, node 2 (Supplemental Movie 1). Representative  $\text{Ca}^{2+}$  traces in  
 155 node 2 for  $d_{\text{shaft}} = d_0$ ,  $\frac{d_0}{2}$  and  $\frac{d_0}{3}$  are displayed in Fig 3A. Our first result is that  $\text{Ca}^{2+}$  peak probability

156 increases when  $d_{\text{shaft}}$  decreases (Fig 3B1). The time to 1<sup>st</sup> peak increases with  $d_{\text{shaft}}$  (Fig 3B2). By con-  
157 trast, peak amplitude (Fig 3B3) and duration (Fig 3B4) increase when  $d_{\text{shaft}}$  decreases. In order to  
158 better understand the mechanisms responsible for the increased  $\text{Ca}^{2+}$  peak probability, amplitude  
159 and duration when  $d_{\text{shaft}}$  decreases, we have measured the frequency of  $IP_3R$  opening in nodes  
160 1 and 2. The frequency of  $IP_3R$  opening increases when  $d_{\text{shaft}}$  decreases (Fig 3B5). Note that the  
161 duration of  $IP_3R$  opening and the number of  $IP_3Rs$  open per  $\text{Ca}^{2+}$  peak did not vary with  $d_{\text{shaft}}$ . The  
162 increased  $IP_3R$  opening frequency associated with small values of  $d_{\text{shaft}}$  probably results from the  
163 increased residency time of molecules in nodes connected to thin shafts (Fig 3C). Indeed, a thin  
164 shaft can "trap"  $\text{Ca}^{2+}$  and  $IP_3$  longer in the node, thus locally increasing the probability of  $IP_3Rs$   
165 to open, resulting in larger  $\text{Ca}^{2+}$  peaks. For more details, the reader can refer to the theoretical  
166 work investigating the narrow escape problem for diffusion in microdomains (*Schuss et al., 2007*).  
167 Nodes connected to thinner shafts, despite being characterized by a lower diffusion flux (Fig 2),  
168 could thus consist of signal amplification units, favoring the generation of larger signals, therefore  
169 increasing  $\text{Ca}^{2+}$  peak probability, amplitude and duration both in the stimulated node and in neigh-  
170 boring nodes.

171

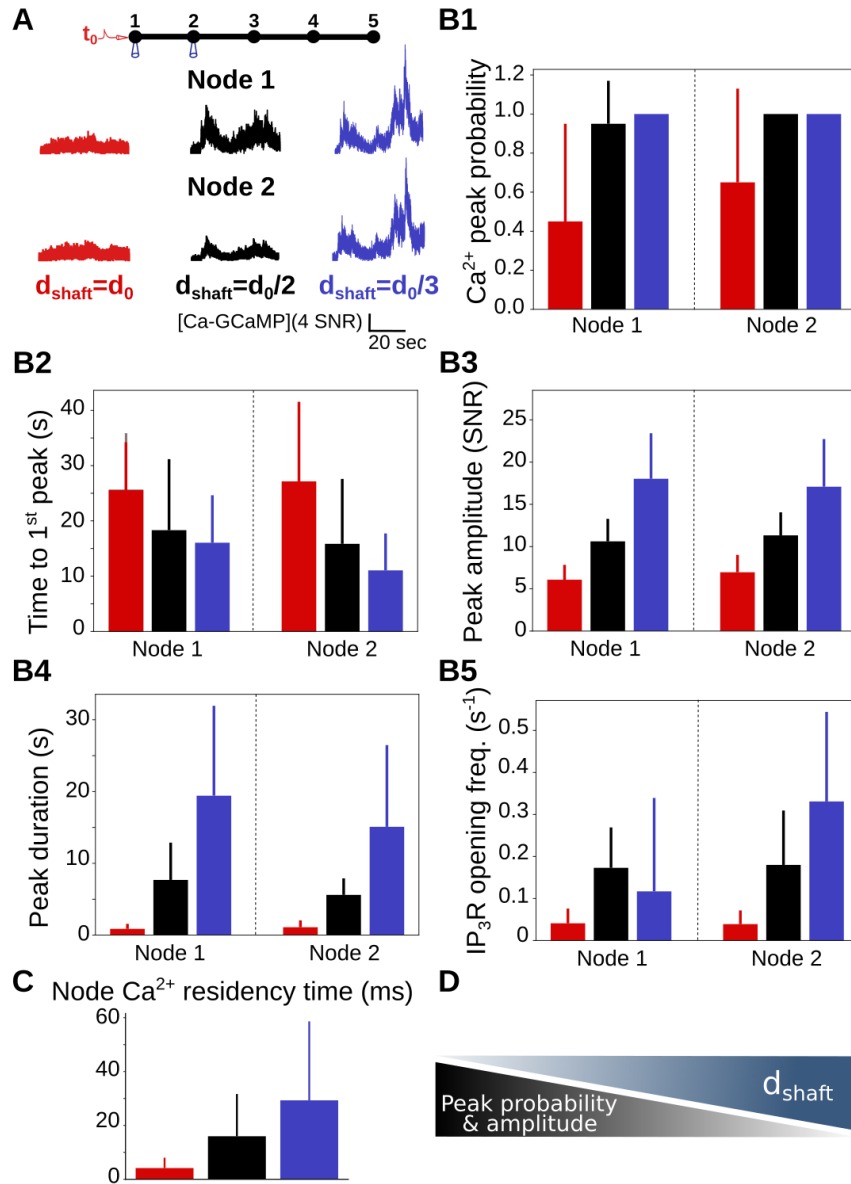


**Figure 3. Ca<sup>2+</sup> peak probability, amplitude and duration increase when shaft width decreases.** (A) (Top) Neuronal stimulation protocol simulated for each geometry: node 1 was stimulated at  $t=t_0=1s$ , while Ca<sup>2+</sup> activity was monitored in node 2. Representative Ca<sup>2+</sup> traces for shaft width  $d_{\text{shaft}} = d_0$  (red),  $\frac{d_0}{2}$  (black) and  $\frac{d_0}{3}$  (blue), expressed as SNR (see Methods). (B) Quantification of the effect of  $d_{\text{shaft}}$  on Ca<sup>2+</sup> signal characteristics. Data are represented as mean  $\pm$  STD,  $n=20$ . Ca<sup>2+</sup> peak probability increases (\*\*\*, B1), Time to 1<sup>st</sup> peak decreases (\*\*\*, B2), peak amplitude (\*\*\*, B3) and duration (\*\*\*, B4) increase when  $d_{\text{shaft}}$  decreases. (C) Ca<sup>2+</sup> residency time in node 1 increases when  $d_{\text{shaft}}$  decreases (\*\*\*,  $n=300$ ). (D) Schematic summarizing the main result from this figure: Ca<sup>2+</sup> peak probability and amplitude increase when shaft width decreases. The effect of  $d_{\text{shaft}}$  on each Ca<sup>2+</sup> signal characteristic was tested using one-way ANOVA. Significance is assigned by \* for  $p \leq 0.05$ , \*\* for  $p \leq 0.01$ , \*\*\* for  $p \leq 0.001$ .

**Figure 3-video 1.** Movie of a simulation of the neuronal stimulation protocol, with  $d_{\text{shaft}} = \frac{d_0}{2}$ ,  $k_{Ca} = 0 s^{-1}$ .

**Figure 3-Figure supplement 1.** Sensitivity study of the effect of  $d_{\text{shaft}}$  on local Ca<sup>2+</sup> signals.

**Figure 3-Figure supplement 2.** Effect of Ca<sup>2+</sup> influx rate at the plasma membrane on local Ca<sup>2+</sup> signals.

**Figure 3-Figure supplement 3.** Sensitivity study of the effect of boundary conditions on local Ca<sup>2+</sup> activity upon single node stimulation.

**Figure 3-Figure supplement 4.** Node/shaft width ratio and node volume control local Ca<sup>2+</sup> activity.

**Figure 3-Figure supplement 5.** Thin shafts enhance local spontaneous Ca<sup>2+</sup> activity.

**Figure 3-Figure supplement 6.** Ca<sup>2+</sup> peak probability, amplitude and duration decrease with ER surface area.

**Figure 3-Figure supplement 7.** Local Ca<sup>2+</sup> activity increases when shaft diameter decreases, for all ER geometries tested.

**Figure 3-Figure supplement 8.** Sensitivity study of the effect of ER morphology on Ca<sup>2+</sup> dynamics.

**Figure 3-Figure supplement 9.** Ca<sup>2+</sup> indicators alter Ca<sup>2+</sup> peak characteristics.

172 To identify the cause of the increased  $\text{Ca}^{2+}$  activity when shaft width decreases ( Fig 3), we per-  
173 formed simulations in which we altered the stimulated node (Supplemental Fig 1 D-E),  $\text{Ca}^{2+}$  influx at  
174 the plasma membrane (Supplemental Fig 2) and boundary conditions (Supplemental Fig 3). Those  
175 parameters did not affect the observed effects of  $d_{\text{shaft}}$  on  $\text{Ca}^{2+}$  dynamics. Furthermore, we re-  
176 peated simulations of Fig 3 with constant cytosolic volume (Supplemental Fig 4) and constant num-  
177 ber of  $\text{IP}_3$ Rs (Supplemental Fig 1 A-C), irrespective of the value of  $d_{\text{shaft}}$ . Our results confirm that the  
178 relevant parameter responsible for the observed effects of  $d_{\text{shaft}}$  on  $\text{Ca}^{2+}$  signal characteristics is  
179 the node/shaft width ratio or the cytosolic volume rather than  $d_{\text{shaft}}$  itself. Spontaneous  $\text{Ca}^{2+}$  sig-  
180 nals were affected by shaft width in the same way as neuronal-induced  $\text{Ca}^{2+}$  signals (Supplemental  
181 Fig 5) and, in particular, reproduced the increase of the amplitude ratio of spontaneous  $\text{Ca}^{2+}$  sig-  
182 nals between node 2 and node 1 with shaft width observed in hippocampal organotypic cultures  
183 (*Arizono et al., 2020*). Note that ER morphology, in particular ER surface area (Supplemental Fig 6,  
184 7 and 8), and  $\text{Ca}^{2+}$  buffering by  $\text{Ca}^{2+}$  indicators (Supplemental Fig 9), consistent with previous re-  
185 ports (*Denizot et al., 2019a; Bartol et al., 2015; Majewska et al., 2000*), can also alter local  $\text{Ca}^{2+}$   
186 dynamics.

187 Overall, our results suggest that a decreased shaft width, resulting in a decreased diffusion ef-  
188 flux from nodes, increases  $\text{Ca}^{2+}$  peak probability, amplitude and duration. Conversely, the swelling  
189 of fine processes, resulting in an increase of shaft width, attenuates local  $\text{Ca}^{2+}$  peak probability,  
190 amplitude and duration.

### 191 $\text{Ca}^{2+}$ imaging confirms that swelling attenuates local spontaneous $\text{Ca}^{2+}$ activity

192 Our recent super-resolution study revealed that the nano-architecture of fine processes is re-  
193 modeled in hypo-osmotic conditions (*Arizono et al., 2021b*). At this spatial scale, hypo-osmotic  
194 conditions resulted in heterogeneous swelling of processes, where shaft width increased while  
195 node width remained unaltered (see Fig 3 in (*Arizono et al., 2021b*)). Simulation results presented  
196 in Fig 3 suggest that processes with increased shaft width  $d_{\text{shaft}}$  are associated with decreased  $\text{Ca}^{2+}$   
197 peak probability, duration and amplitude. To test whether this effect can be observed in live tis-  
198 sue, we thus performed experimental measurements of calcium dynamics in fine astrocytic pro-  
199 cesses under basal and hypo-osmotic conditions. To resolve  $\text{Ca}^{2+}$  signals in fine branchlets, we  
200 performed experiments using confocal microscopy in organotypic cultures, which provides the  
201 best optical access and sample stability in live tissue to date (resolution  $\approx 200$  nm in x-y versus  $\approx$   
202 500 nm for two-photon microscopy). In accordance with our model's predictions,  $\text{Ca}^{2+}$  peak ampli-  
203 tude and duration were lower in hypo-osmotic compared to basal conditions (Fig 4A-D). Note that  
204 peak amplitude and duration did not significantly vary when measured repeatedly in basal condi-  
205 tions (Fig 4E-F). Overall, our experimental results confirm that the complex nano-architecture of  
206 fine astrocytic processes and its alteration, such as cell swelling, shapes local  $\text{Ca}^{2+}$  activity.

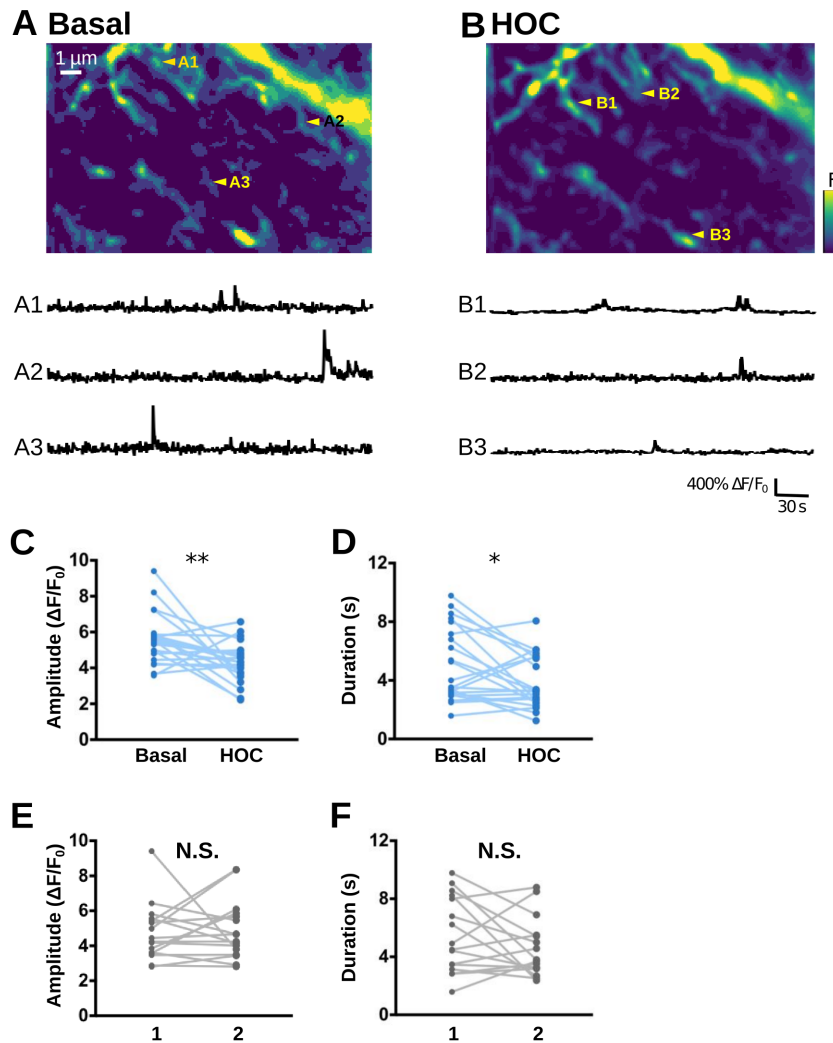


**Figure 4. Ca<sup>2+</sup> imaging confirms that swelling attenuates local spontaneous Ca<sup>2+</sup> activity.** (A, B) (Top) Confocal images of the astrocytic spongiform domain expressing GCaMP6s at baseline (basal, A) and in hypo-osmotic condition (HOC, B), measured in organotypic hippocampal cultures. (Bottom) Representative traces of spontaneous Ca<sup>2+</sup> events from ROIs indicated in A (A1-A3) and B (B1-B3). (C, D) Ca<sup>2+</sup> peak amplitude (C) and duration (D) of spontaneous Ca<sup>2+</sup> events are significantly smaller in hypo-osmotic conditions (HOC) compared to basal conditions (Basal). (E, F) Amplitude (E) and duration (F) of spontaneous Ca<sup>2+</sup> events do not significantly vary when measured twice in a row (1, 2) in the absence of HOC. Significance is assigned by \* for  $p \leq 0.05$ , \*\* for  $p \leq 0.01$ , \*\*\* for  $p \leq 0.001$ .

### Thin shafts favor more robust signal propagation

207 A single astrocyte branchlet can contact and modulate the activity of multiple synapses, re-  
 208 ferred to as synaptic clusters, which can belong to the same or to different dendrites or even to  
 209 different neurons (Arizono et al., 2020; Reichenbach et al., 2010; Witcher et al., 2007; Cali et al.,  
 210 2019; Semyanov et al., 2020). The frequency of stimulation of the branchlet can vary depending  
 211 on the activity of the adjacent synapses. For example, a connection of adjacent astrocytic nodes  
 212 to co-active synapses would result in a high node stimulation frequency. We have thus tested the  
 213 influence of the frequency of neuronal stimulation of neighboring nodes on the propagation of  
 214 Ca<sup>2+</sup> signals in branchlets. To do so, we have performed simulations in which neighboring nodes  
 215 were repeatedly stimulated after a time period  $\tau_{IP_3}$ , that varied from 50 ms to 5s, while Ca<sup>2+</sup> signals  
 216 were recorded in a remote node, node 5 (Fig 5A). Neuronal stimulation is simulated as an infusion  
 217 of 50 IP<sub>3</sub> molecules in the stimulated node. Representative Ca<sup>2+</sup> traces in node 5 in branchlets with  
 218

219 various shaft widths  $d_{\text{shaft}}$  are presented in Fig 5A for  $\tau_{\text{IP3}}=250$  and 3000 ms. Our first notable result  
220 is that the time to 1<sup>st</sup> peak in node 5 decreases with  $d_{\text{shaft}}$ , whatever the value of  $\tau_{\text{IP3}}$  (Fig 5B1). More  
221 specifically, time to 1<sup>st</sup> peak is higher for  $d_{\text{shaft}}=d_0$  compared to both  $d_{\text{shaft}}=\frac{d_0}{2}$  and  $\frac{d_0}{3}$ , while differ-  
222 ences between  $d_{\text{shaft}}=\frac{d_0}{2}$  and  $\frac{d_0}{3}$  are not as striking. Moreover, the difference between  $d_{\text{shaft}}=d_0$ ,  $\frac{d_0}{2}$   
223 and  $\frac{d_0}{3}$  increases with  $\tau_{\text{IP3}}$ . This suggests that geometries with  $d_{\text{shaft}}=d_0$  better discriminate slow from  
224 fast frequency of node stimulation compared to geometries with thinner shafts. Geometries with  
225  $d_{\text{shaft}}=d_0$  are further characterized by a lower  $\text{Ca}^{2+}$  peak probability in node 5 compared to geome-  
226 tries with  $d_{\text{shaft}}=\frac{d_0}{2}$  and  $\frac{d_0}{3}$  (Fig 5B2). More precisely,  $\text{Ca}^{2+}$  peak probability decreases as  $\tau_{\text{IP3}}$  increases  
227 for  $d_{\text{shaft}}=d_0$ , which was observed independently of our boundary conditions (Supplemental Fig 1,  
228 see Methods). This suggests that geometries with larger shafts could be associated with decreased  
229 signal propagation to remote nodes in case of repeated node stimulation at low frequency ( $\tau_{\text{IP3}} >$   
230 2s).

231

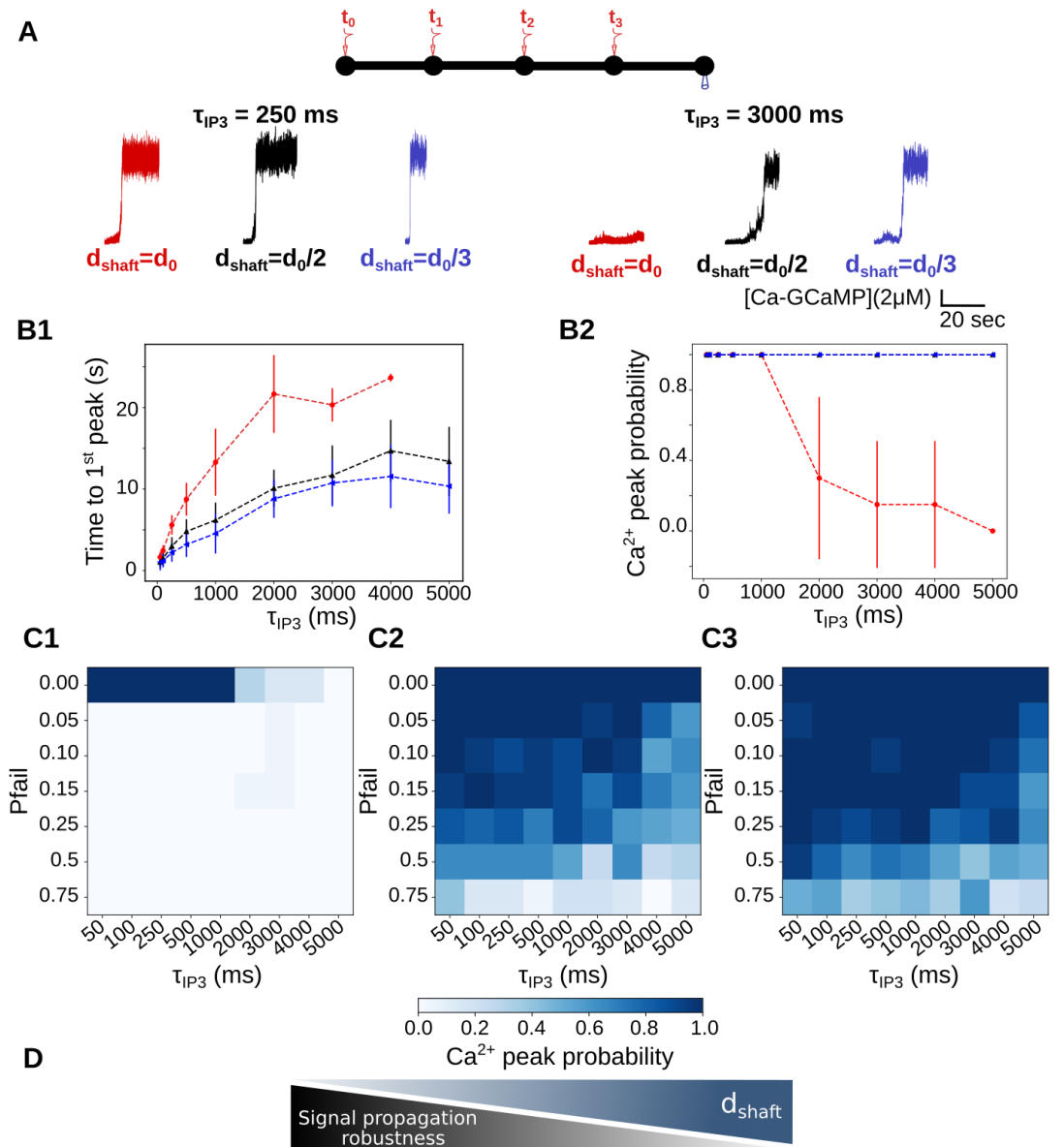


**Figure 5. Thin shafts are associated with a more robust signal propagation upon repeated neuronal stimuli.** (A) (Top) Neuronal stimulation protocol: node 1 is stimulated at  $t=t_0=5s$ , node 2 at  $t_0 + \tau_{IP3}$ , node 3 at  $t_0 + 2\tau_{IP3}$  and node 4 at  $t_0 + 3\tau_{IP3}$ ,  $k_{Ca}=0 \text{ s}^{-1}$ .  $Ca^{2+}$  activity is recorded in node 5. (Bottom) Representative  $Ca^{2+}$  traces in node 5 for shaft width  $d_{shaft} = d_0$  (red),  $\frac{d_0}{2}$  (black) and  $\frac{d_0}{3}$  (blue), with  $\tau_{IP3}=250\text{ms}$  (left) and  $3000\text{ms}$  (right), expressed as SNR (see Methods). (B1) Time to 1<sup>st</sup> peak increases with  $\tau_{IP3}$  for  $d_{shaft} = d_0$  (\*\*\*),  $\frac{d_0}{2}$  (\*\*\*), and  $\frac{d_0}{3}$  (\*\*\*). T-tests revealed that for any value of  $\tau_{IP3}$ , time to 1<sup>st</sup> peak is higher for  $d_{shaft} = d_0$  compared to  $d_{shaft} = \frac{d_0}{2}$  and  $\frac{d_0}{3}$ . Time to 1<sup>st</sup> peak is significantly higher when  $d_{shaft} = \frac{d_0}{2}$  compared to  $d_{shaft} = \frac{d_0}{3}$ , for most values of  $\tau_{IP3}$  ( $p=0.032^*$ ,  $0.0025^{**}$ ,  $0.034^*$ ,  $0.016^*$  and  $0.019^*$  for  $\tau_{IP3}=250, 500, 1000, 4000$  and  $5000$ , respectively). (B2)  $Ca^{2+}$  peak probability in node 5 is lower for  $d_{shaft} = d_0$  compared to  $d_{shaft} = \frac{d_0}{2}$  and  $\frac{d_0}{3}$ .  $Ca^{2+}$  peak probability decreases as  $\tau_{IP3}$  increases for  $d_{shaft} = d_0$  (\*\*\*). (C)  $Ca^{2+}$  peak probability in node 5 (colorbar) as a function of  $\tau_{IP3}$  and of the probability of failure of node stimulation  $p_{fail}$ , for  $d_{shaft} = d_0$  (C1),  $d_{shaft} = \frac{d_0}{2}$  (C2) and  $d_{shaft} = \frac{d_0}{3}$  (C3), with  $p_{fail} \in [0, 1]$ . (D) Schematic summarizing the main conclusion of this figure: decreased shaft width allows signal propagation despite omitted node stimulation, thus favoring more robust signal propagation. Data are represented as mean  $\pm$  STD,  $n=20$  for each value of  $d_{shaft}$  and of  $\tau_{IP3}$ . Lines in panel B are guides for the eyes. The effect of  $d_{shaft}$  on each  $Ca^{2+}$  signal characteristic was tested using one-way ANOVA. Significance is assigned by \* for  $p \leq 0.05$ , \*\* for  $p \leq 0.01$ , \*\*\* for  $p \leq 0.001$ .

**Figure 5-Figure supplement 1.** Sensitivity study of the effect of boundary conditions on local  $Ca^{2+}$  activity upon repeated neuronal stimuli.

232 For  $\tau_{IP3}=4s$  and  $d_{\text{shaft}}=\frac{d_0}{3}$ , signals were detected in node 5  $11.55 \pm 3.89$  s after the stimulation of  
233 node 1, which means that they occurred before the stimulation of node 4 ( $t=t_0 + 12s$  for  $\tau_{IP3}=4s$ ).  
234 This phenomenon was not observed for  $d_{\text{shaft}}=d_0$ , for which time to 1<sup>st</sup> peak when  $\tau_{IP3}=4s$  was  $23.67$   
235  $\pm 0.47$  s. This suggests that for  $d_{\text{shaft}}=\frac{d_0}{3}$ , contrary to  $d_{\text{shaft}}=d_0$ , one node stimulation could be omitted  
236 without having any consequence on  $Ca^{2+}$  peak probability in node 5. In order to test this hypothesis,  
237 we have performed simulations in which the stimulation of nodes 2, 3 and 4 occurred with a given  
238 probability of failure  $p_{\text{fail}}$ . Simulations were performed for  $p_{\text{fail}}=0, 0.05, 0.1, 0.15, 0.25$  and  $0.75$ .  $Ca^{2+}$   
239 peak probability in node 5, depending on  $p_{\text{fail}}$  and on  $\tau_{IP3}$  is presented in Fig 5C, for  $d_{\text{shaft}}=d_0$  (Fig 5C1),  
240  $d_{\text{shaft}}=\frac{d_0}{2}$  (Fig 5C2) and  $d_{\text{shaft}}=\frac{d_0}{3}$  (Fig 5C3). As expected,  $Ca^{2+}$  peak probability, despite high values of  
241  $p_{\text{fail}}$ , increases when  $d_{\text{shaft}}$  decreases. Thus, thin shafts can favor signal propagation by allowing the  
242 omission of a node stimulation. In that sense, geometries displaying thin shafts are characterized  
243 by a more robust signal propagation (Fig 5D).

244  
245 Together, our results suggest that, in the context of repeated node stimulation, thin shafts are  
246 associated with an increase of  $Ca^{2+}$  peak probability in more remote nodes, with an earlier sig-  
247 nal onset, suggesting increased signal propagation. Astrocytic processes with thicker shafts (here  
248  $d_{\text{shaft}}=d_0$ ), such as observed in hypo-osmotic conditions (*Arizono et al., 2021b*), are associated with  
249 lower signal propagation in case of low stimulation frequency (time period  $> 2s$ ), potentially fa-  
250 voring the formation of local  $Ca^{2+}$  hotspots. Our results suggest that geometries with thick shafts  
251 could impair signal propagation when a branchlet is stimulated at a low frequency. In that sense,  
252 astrocyte branchlets with thicker shafts would be better detectors of the surrounding level of neu-  
253 ronal activity. By contrast, branchlets with thin shafts would be less discriminating and provide  
254 more robust signal propagation.

## 255 Discussion

256 Fine astrocytic processes are responsible for most astrocytic  $Ca^{2+}$  signals (*Bindocci et al., 2017*)  
257 and are preferential sites of neuron-astrocyte communication (*Arizono et al., 2020*). A better un-  
258 derstanding of the mechanistic link between their morphology and the spatio-temporal properties  
259 of local  $Ca^{2+}$  signals is crucial, yet hard to test experimentally. Here, we perform reaction-diffusion  
260 simulations in idealized morphologies of astrocytic processes derived from 3D super-resolution mi-  
261 croscopy to investigate the effect of astrocyte nanoscale morphology on  $Ca^{2+}$  activity in the gliapil.  
262 Our simulation results suggest that the morphology of processes, alternating between large and  
263 thinner cellular compartments (*Panatier et al., 2014; Arizono et al., 2020; Grosche et al., 1999*), in-  
264 creases  $Ca^{2+}$  peak probability, duration, amplitude and propagation. Conversely, astrocyte swelling  
265 attenuates local  $Ca^{2+}$  activity and signal propagation (Fig 6). Our simulation results, in accordance  
266 with experimental data, suggest that thin shafts are associated with a decreased diffusion flux, i.e  
267 an increased compartmentalization of nodes. Thus, nodes, similarly to dendritic spines (*Santa-*  
268 *maria et al., 2011*), act as diffusion traps when shaft width is low. Note that, more than the value  
269 of shaft width itself, our results emphasize the effect of the ratio between node and shaft diameter  
270 on  $Ca^{2+}$  activity. The geometries designed and used in this study emerge as interesting tools to in-  
271 vestigate the influence of the ultrastructure of fine astrocyte branchlets on the local  $Ca^{2+}$  dynamics  
272 in health and disease. By recording the mechanisms resulting in  $Ca^{2+}$  signals upon neuronal stim-  
273 ulation in small cellular compartments of the gliapil, which cannot be performed experimentally,  
274 our simulation results shed light on the mechanisms by which astrocyte swelling influences the  
275 frequency, amplitude and propagation of  $Ca^{2+}$  signals at the nanoscale.

276

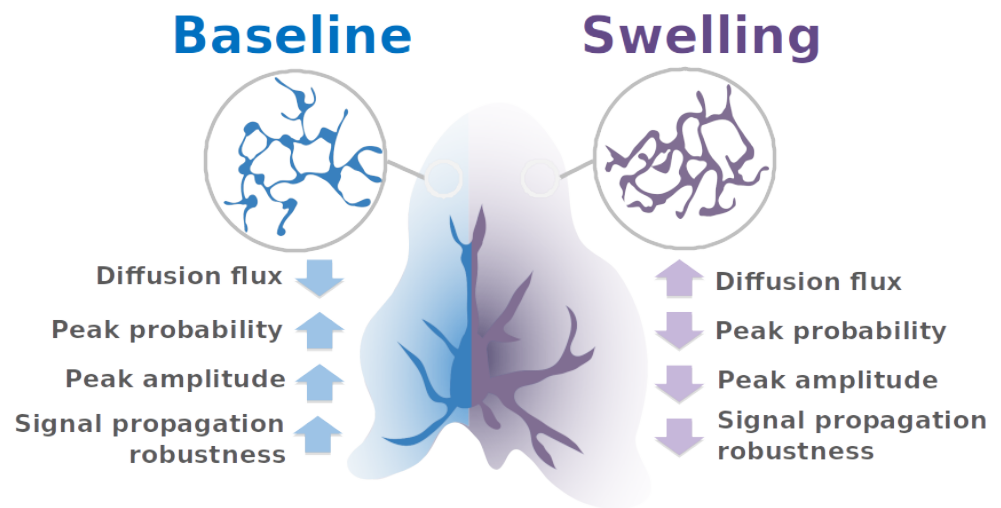


**Figure 6. Proposed mechanisms that regulate astrocytic  $\text{Ca}^{2+}$  activity at tripartite synapses.** Our simulation results demonstrate that the nano-morphology of astrocytic processes, consisting in the alternation of nodes and shafts, powerfully shapes the spatio-temporal properties of  $\text{Ca}^{2+}$  signals and promotes local  $\text{Ca}^{2+}$  activity. Astrocyte swelling, observed in pathological conditions such as brain injury, stroke and epilepsy, results in an increased shaft width without altering node size. Our results suggest that such pathological alterations of the nanoscale morphology of astrocytes result in a decreased local  $\text{Ca}^{2+}$  activity, which we confirm experimentally in hypo-osmotic conditions. Upon repeated neuronal stimuli, we predict that swelling hinders astrocytic signal propagation. Overall, this study highlights the impact of astrocyte nano-morphology on astrocyte activity at tripartite synapses, in health and disease.

277 Experimental  $\text{Ca}^{2+}$  recordings of astrocyte activity have established that astrocyte processes display both highly localized microdomain signals and propagating  $\text{Ca}^{2+}$  waves (*Srinivasan et al., 2015;*  
 278 *Bindocci et al., 2017*). Our simulations suggest that the morphology of the cell and of its organelles  
 279 can strongly influence the formation of these patterns of astrocytic  $\text{Ca}^{2+}$  signaling. Notably, thinner  
 280 shafts allow less discriminating and more robust signal propagation upon repeated stimuli compared  
 281 to larger shafts. Thinner shafts indeed allow signal propagation even in the absence of some  
 282 stimuli or when the time interval between repeated stimuli is large. On the contrary, geometries  
 283 with thick shafts seem to be more discriminating, potentially favoring the propagation of signals  
 284 resulting from repeated stimuli from co-active synapses. Cellular morphology thus emerges as  
 285 a key parameter that regulates the active propagation of  $\text{Ca}^{2+}$  signals. The ultrastructure of the  
 286 spongiform domain of astrocytes is very complex, characterized by abundant branching points,  
 287 conferring a reticular morphology (*Arizono et al., 2020*). Those branching points are reportedly  
 288 sometimes arranged into ring-like structures, although their occurrence and shape are still debated  
 289 and could differ depending on the brain region under study (*Arizono et al., 2020; Panatier*  
 290 *et al., 2014; Kiyoshi et al., 2020; Salmon et al., 2021; Arizono and Nägerl, 2021*). The effect of this  
 291 reticular ultrastructure on the propagation of  $\text{Ca}^{2+}$  signals remains to be uncovered. Further characterization  
 292 of the shape of fine astrocytic processes of the spongiform domain, their variability  
 293 as well as their connectivity to the neighboring synapses are thus required. Pairing those observations  
 294 with biophysically-detailed models such as the one presented in this study stands to deepen  
 295 our understanding of the roles of astrocytic and neuronal morphology at tripartite synapses on  
 296 neuron-astrocyte communication.  
 297

298  
 299 In neurons, both experimental (*Yuste et al., 2000; Noguchi et al., 2005; Tønnesen et al., 2014*)  
 300 and modelling (*Schmidt and Eilers, 2009; Biess et al., 2007; Simon et al., 2014; Bell et al., 2019; Hol-*  
 301 *cman and Schuss, 2005, 2011; Santamaria et al., 2011; Cugno et al., 2019*) studies have suggested  
 302 that thin spine necks favor the compartmentalization of  $\text{Ca}^{2+}$  signals within the spine head. This  
 303 compartmentalization of synapses allows neurons to discriminate various inputs and to process

304 information locally (*Wybo et al., 2019; Poirazi and Papoutsis, 2020*), increasing the computational  
305 power of the neuronal circuits. According to our simulation results, nodes connected to thin shafts  
306 could favor the emergence of large signals at the site of neuron-astrocyte communication. Interest-  
307 ingly, we further propose that those amplified signals in nodes, instead of resulting in  $\text{Ca}^{2+}$  hotspots,  
308 favor active signal propagation. In response to spike timing-dependent plasticity (STDP) protocols  
309 (*Araya et al., 2014*) and after long-term potentiation (*Tønnesen et al., 2014*), the neck of dendritic  
310 spines become wider and shorter. Recent *in vitro* and *in vivo* studies have reported that the geom-  
311 etry of the ER in neurons is also highly dynamic (*Kucharz et al., 2013*), experiencing fast fission and  
312 fusion events. Further, the ER is variably distributed in spines, being preferentially present in large  
313 spines associated with strong synapses (*Holbro et al., 2009*). The geometries of dendrites and of  
314 their organelles, which influence local signals, are thus highly dynamic. Similarly, fine astrocytic  
315 processes encounter morphological rearrangements that are activity-dependent, which notably  
316 influence synaptic maturation, efficacy and spine stability (*Theodosis et al., 2008; Zhou et al., 2019;*  
317 *Henneberger et al., 2020*). Our study sheds light on the influence of rearrangements of the reticular  
318 morphology of fine processes on signal computation by astrocytes. Further investigation manipu-  
319 lating astrocyte morphology *in situ* as well as *in vivo* is required to better characterize the variability  
320 of astrocyte ultrastructure and the associated integration of  $\text{Ca}^{2+}$  signals.

321  
322 The morphology of the complex spongiform domain of astrocytes is highly dynamic, subject to  
323 activity-dependent as well as pathological remodeling. Our study, providing mechanisms by which  
324 an altered astrocyte morphology influences neuron-astrocyte communication at the nanoscale,  
325 gives new insights into the involvement of astrocytes in brain function in health and disease.

## 326 **Methods and Materials**

### 327 **Stochastic spatially-explicit voxel-based simulations**

328 In order to model astrocyte  $\text{Ca}^{2+}$  signals in astrocyte branchlets, we have used the voxel-based  
329 “GCaMP” implementation of the Inositol 3-Phosphate ( $\text{IP}_3$ ) receptor-dependent  $\text{Ca}^{2+}$  signaling model  
330 from Denizot et al (*Denizot et al., 2019a*), using the same reaction scheme and parameter values  
331 (Fig 1B). Briefly, we model  $\text{Ca}^{2+}$  fluxes in and out of the cytosol, mediated by  $\text{Ca}^{2+}$  channels and  
332 pumps on the endoplasmic reticulum (ER) and on the plasma membrane.  $\text{Ca}^{2+}$  signals occur when  
333 some  $\text{IP}_3$ R channels are in the open state.  $\text{IP}_3$  can be synthesized by the  $\text{Ca}^{2+}$ -dependent activ-  
334 ity of phospholipase C  $\delta$  ( $\text{PLC}\delta$ ) and the removal of  $\text{IP}_3$  molecules from the cytosol is expressed  
335 as a single decay rate.  $\text{IP}_3$ R kinetics is described by a Markov model, derived from De Young &  
336 Keizer’s model (*De Young and Keizer, 1992*). Each  $\text{IP}_3$ R molecule contains one  $\text{IP}_3$  binding site and  
337 two  $\text{Ca}^{2+}$  binding sites. An  $\text{IP}_3$ R is in the open state when in state {110} (first Ca site and  $\text{IP}_3$  bound,  
338 second Ca site free). Depending on the simulation, other diffusing molecules were added to the  
339 model, such as the fluorescent molecule ZsGreen and fluorescent  $\text{Ca}^{2+}$  indicators, here 10  $\mu\text{M}$  of  
340 GCaMP6s. GCaMPs are genetically-encoded  $\text{Ca}^{2+}$  indicators (GECIs) that are derived from the flu-  
341 orescent protein GFP and the  $\text{Ca}^{2+}$  buffer calmodulin (see (*Shigetomi et al., 2016*) for a review on  
342 GECIs). For further details on the kinetic scheme and model assumptions, please refer to Denizot  
343 et al. 2019 (*Denizot et al., 2019a*).

344  
345 The model was implemented using STEPS (<http://steps.sourceforge.net/>), a python package per-  
346 forming exact stochastic simulation of reaction-diffusion systems (*Hepburn et al., 2012*). More  
347 precisely, STEPS uses a spatialized implementation of Gillespie’s SSA algorithm (*Gillespie, 1977;*  
348 *Isaacson and Isaacson, 2009; Smith and Grima, 2018*). Simulations in STEPS can be performed in  
349 complex geometries in 3 spatial dimensions. Space is divided into well-mixed tetrahedral compart-  
350 ments, referred to as voxels. Reactions between 2 molecules can only occur if they are located  
351 within the same voxel. Diffusion events are modeled as a decrease of the number of molecules in  
352 the original voxel and an increase in the number of molecules in its neighboring voxel. Boundary

353 conditions, except when specified otherwise, were reflective. In other words, mobile molecules  
354 could not diffuse away from the geometry, as if they were “bouncing” onto the plasma membrane.  
355 STEPS enables to compute, in complex 3D geometries, reactions and diffusion in the cytosol as well  
356 as reactions between cytosolic molecules and molecules located at the plasma or ER membrane.

357

## 358 Geometries

359 Typical astrocyte branchlet geometries were designed from their recent experimental charac-  
360 terization in live tissue at high spatial resolution (50 nm in x-y) (*Arizono et al., 2020*). Those geome-  
361 tries consist in alternations of bulbous structures, nodes, connected to each other with cylindrical  
362 structures, shafts. Geometries with different shaft widths  $d_{\text{shaft}}$  were designed using Trelis software  
363 (<https://www.csimsoft.com/trelis>, Fig 1A). The geometry of a node was approximated as being a  
364 sphere of diameter 380 nm. Shaft geometry consisted in a 1  $\mu\text{m}$  long cylinder. Shaft diameter was  
365 defined relative to node diameter. For example, shaft diameter was the same as node diameter, i.e  
366  $d_{\text{shaft}} = d_0 = 380$  nm. Similarly, shaft diameter was 190 nm and 127 nm for  $d_{\text{shaft}} = \frac{d_0}{2}$  and  $\frac{d_0}{3}$ , respectively.  
367 Cones were positioned between spheres and cylinders in order to create a smoother transition be-  
368 tween nodes and shafts, better approximating the geometry observed experimentally. Cytosolic  
369 volume was thus  $V_1 = 0.620 \mu\text{m}^3$ ,  $V_2 = 0.263 \mu\text{m}^3$  and  $V_3 = 0.195 \mu\text{m}^3$ , for  $d_{\text{shaft}} = d_0$ ,  $\frac{d_0}{2}$  and  $\frac{d_0}{3}$ , respectively.  
370 A subset of simulations were performed in a geometry with  $V_1 = 0.258 \mu\text{m}^3$ . This geometry is charac-  
371 terized, similarly to geometries with  $d_{\text{shaft}} = d_0$ , by a node/shaft width ratio of 1. It contains cylinders  
372 of length 750 nm, diameter 285 nm and spheres of diameter 285 nm. As a first approximation,  
373 ER geometry was considered to be similar to the geometry of the astrocyte branchlet: node/shaft  
374 successions. ER nodes were aligned with cytosolic nodes. As no quantification of the ER volume  
375 compared to cellular volume was found for astrocytes in the literature, ER volume was 10% of the  
376 total branchlet volume, based on available data in neurons (*Spacek and Harris, 1997*). The cytosolic  
377 volume, plasma and ER membrane areas of the different “5Nodes” geometries are presented in  
378 Table 1.

379

380 A sensitivity study was performed to investigate the effect of voxel size on the kinetics of the  
381 molecular interactions modeled. Information on the voxel sizes of the different meshes used is  
382 presented in Supplemental Table 1. Results are presented in Supplemental Fig 1. Meshes that  
383 contained voxels that were  $< 50 \text{ nm}^3$  were characterized by aberrant kinetics, resulting in aberrant  
384 average numbers of molecules in a given state. Those results thus suggest that to prevent errors  
385 due to voxel size, meshes should not display voxel sizes that are  $< 50 \text{ nm}^3$ . We have thus made  
386 sure, while meshing the geometries in which simulations were ran, that no voxels were  $< 50 \text{ nm}^3$ .  
387 Minimum voxel size was 443  $\text{nm}^3$ , 1100  $\text{nm}^3$  and 447  $\text{nm}^3$ , for  $d_{\text{shaft}} = d_0$ ,  $\frac{d_0}{2}$  and  $\frac{d_0}{3}$  geometries, re-  
388 spectively.

389

390 In a subset of simulations, ER geometry varied. The shape of the cell was the same as in “5nodes”  
391 geometries (Fig 1). ER geometry consisting of node/shaft alternations, described above, is referred  
392 to as “Node/shaft ER”. “No ER” geometry contains no ER. “Node ER” is characterized by a discon-  
393 tinuous ER geometry, consisting in spheres of diameter 54 nm, located in cellular nodes. “Cyl ER”  
394 corresponds to a cylindrical ER, of length  $l_{\text{ER}} = 6274$  nm and a diameter of 108, 54 and 36 nm, for  
395  $d_{\text{shaft}} = d_0$ ,  $\frac{d_0}{2}$  and  $\frac{d_0}{3}$ , respectively. The associated cytosolic volume, ER and plasma membrane area  
396 are presented in Table 1.

## 397 Protocol for simulating bleaching experiments

398 In order to test whether the idealized geometries presented in Fig 1 are a good approximation  
399 of the spongiform ultrastructure of astrocyte branchlets, we have simulated their fluorescence  
400 recovery after photobleaching (FRAP) experiments. Briefly, laser pulses are simulated on a node  
401 (region of interest) while the fluorescence level is being recorded. At bleaching time, the fluores-

402 cence level in the region of interest decreases to  $I_0$ . Then, because of the diffusion of fluorescent  
 403 molecules into the region of interest, fluorescence increases until it reaches a new steady state,  
 404  $I_{inf}$ . We characterize node compartmentalization by measuring the time  $\tau$  taken by fluorescing  
 405 molecules to diffuse into the node to reach  $I_{inf}$ . In other words, a high node compartmentalization  
 406 will be associated with a high value of  $\tau$ . Thus, 3 main parameters characterize bleaching traces:  
 407  $I_0$ ,  $\tau$  and  $I_{inf}$ .

408  
 409 To mimic bleaching experiments in fine branchlets performed by Arizono et al (Arizono et al.,  
 410 2020), ZsGreen molecules were added to simulation space. After 2 seconds of simulation, providing  
 411 the basal level of fluorescence, 60% of ZsGreen molecules were bleached. In order to fit  $I_0$  and  $I_{inf}$   
 412 that were measured experimentally, and as bleaching time lasted 10 ms in experiments and 1  
 413 ms in simulations, the bleached volume in simulations was adjusted depending on the geometry  
 414 (see Fig 2A). Bleaching was simulated as a transition from ZsGreen molecules to ZsGreen-bleached  
 415 molecules, the latter being considered as non-fluorescing molecules. Screenshots of simulations,  
 416 illustrating the diffusion of ZsGreen and ZsGreen-bleached molecules, are presented in Fig S2B.  
 417 The number of ZsGreen molecules in the central node was recorded over simulation time and a fit  
 418 was performed following equation 1 to determine the values of  $I_0$ ,  $I_{inf}$  and  $\tau$ .

$$I(t) = I_0 - (I_0 - I_{inf})e^{-t/\tau} \quad (1)$$

419 , where  $I(t)$  is the level of fluorescence measured at time  $t$ . The coefficient of diffusion,  $D_{ZsGreen}$ , and  
 420 the concentration,  $[ZsGreen]$ , of ZsGreen were adjusted to fit experimental data. Indeed, the am-  
 421 plitude of  $[ZsGreen]$  fluctuations at steady state is inversely proportional to the number of ZsGreen  
 422 molecules in the geometry. In other words, fluorescence signals are more noisy when  $[ZsGreen]$   
 423 is low. Moreover, the autocorrelation of those fluctuations depends on the coefficient of diffusion  
 424 of ZsGreen,  $D_{ZsGreen}$ . If  $D_{ZsGreen}$  increases, the autocorrelation of Lag, where Lag is the autocorrela-  
 425 tion delay, will decrease faster as Lag increases. Comparing the fluctuations of  $[ZsGreen]$  and its  
 426 autocorrelation in experiments and in simulations thus enabled to find the values of  $D_{ZsGreen}$  and  
 427 of  $[ZsGreen]$  that allowed for the best fit to experimental data. In the simulations presented here,  
 428  $D_{ZsGreen} = 90 \mu m^2 \cdot s^{-1}$  and  $[ZsGreen] = 25 \mu M$ .

### 429 **Protocols for simulating neuronal stimulation**

430 In order to investigate the propagation of  $Ca^{2+}$  signals from nodes that contact neuronal spines,  
 431 we have developed 2 different protocols for our simulations, performed in the geometries pre-  
 432 sented in Fig 1. As nodes were the site of  $Ca^{2+}$  signal initiation (Arizono et al., 2020) and as most  
 433 spines contacted nodes rather than shafts, we have simulated neuronal stimulation in nodes. To  
 434 simulate neuronal stimulation,  $IP_3$  and  $Ca^{2+}$  were infused in the cytosol at stimulation time.  $IP_3$   
 435 infusion reflects the production of  $IP_3$  by phospholipase C that results from the activation of  $G_q$ -G-  
 436 protein-coupled receptors (GPCRs).  $Ca^{2+}$  infusion mimics the influx of  $Ca^{2+}$  in the cytosol through  
 437  $Ca^{2+}$  channels at the plasma membrane. The rate of this neuronal activity-induced  $Ca^{2+}$  influx,  $k_{Ca}$ ,  
 438 varied within a physiological range of values, from 0 to  $1000 s^{-1}$  (Wu et al., 2018; Brazhe et al., 2018).  
 439 Signals were recorded both in the stimulated node, Node 1, and in the neighboring node, Node 2.

- 440 • In the first protocol, 100  $IP_3$  molecules were infused in Node 1, at  $t=t_0=1s$ , while  $Ca^{2+}$  activity  
 441 was monitored in Node 1 and in the neighboring node, Node 2 (see e.g Fig 3A). Neuronal  
 442 activity-induced  $Ca^{2+}$  influx was mediated by generic  $Ca^{2+}$  channels at the plasma membrane.  
 443 25 of those  $Ca^{2+}$  channels were placed on the plasma membrane of Node 1, corresponding  
 444 to a similar density to the  $IP_3R$  density on the ER membrane, and were set to an inactive state.  
 445 At stimulation time  $t=t_0$ ,  $Ca^{2+}$  channels were set to an active state, resulting in an influx of  $Ca^{2+}$   
 446 within the cytosol at rate  $k_{Ca}$ . At  $t=t_0 + 1$ ,  $Ca^{2+}$  channels were set back to their initial inactive  
 447 state. Simulations were performed in geometries with varying shaft width  $d_{shaft}$ .

448 • In the second protocol, we have investigated signal propagation in the node/shaft geometry  
449 depending on shaft width  $d_{\text{shaft}}$  when several nodes were successively stimulated. In “5nodes”  
450 geometries, 50 IP<sub>3</sub> molecules were infused at  $t_0=5s$ ,  $t_0 + \tau_{\text{IP}_3}$ ,  $t_0 + 2\tau_{\text{IP}_3}$ ,  $t_0 + 3\tau_{\text{IP}_3}$  in Nodes 1, 2,  
451 3 and 4, respectively. During the whole simulation time, Ca<sup>2+</sup> activity was recorded in Node  
452 5 (see Fig 5). In a subset of simulations, stimulation of Nodes 2, 3 and 4 occurred with a  
453 probability  $1 - p_{\text{fail}}$ , with  $p_{\text{fail}} \in [0, 1]$ .

#### 454 **Peak detection and analysis**

455 The same strategy as developed by Denizot et al. (*Denizot et al., 2019a*) was used for detect-  
456 ing and analysing Ca<sup>2+</sup> signals. Briefly, basal concentration of Ca<sup>2+</sup>,  $[Ca]_b$ , was defined based on a  
457 histogram of the number of Ca<sup>2+</sup> ions in the absence of neuronal stimulation. Peak initiation cor-  
458 responded to the time when  $[Ca^{2+}]$  was higher than the following threshold:  $[Ca]_b + n\sigma_{Ca}$ , where  $\sigma_{Ca}$   
459 is the standard deviation of  $[Ca^{2+}]$  histogram in the absence of neuronal stimulation. The value of  
460  $n$  was set by hand depending on signal/noise ratio of the simulation of interest. Peak termination  
461 corresponded to the time when  $[Ca^{2+}]$  decreased below the peak threshold.

462 Several parameters were analyzed to characterize Ca<sup>2+</sup> signals. Peak amplitude,  $A$ , corresponds to  
463 the maximum  $[Ca^{2+}]$  measured during the peak duration. It is expressed as signal to noise ratio  
464  $SNR = \frac{A - [Ca]_b}{[Ca]_b}$ . Peak duration corresponds to the time between peak initiation and peak termi-  
465 nation. Time to 1<sup>st</sup> peak corresponds to the delay between the beginning of the simulation and  
466 the first peak detection, measured in the cellular compartment of interest. Peak probability corre-  
467 sponds to the fraction of simulations in which at least one peak was detected during simulation  
468 time in the region of interest. Ca<sup>2+</sup> residency time was measured by performing  $n=300$  simulations  
469 for each value of  $d_{\text{shaft}}$ , in which only 1 Ca<sup>2+</sup> ion was added to node 1, without other molecular  
470 species. Ca<sup>2+</sup> residency time corresponds to the time taken for the ion to diffuse away from node  
471 1.

#### 472 **Organotypic hippocampal slice cultures**

473 All experiments were performed as described in (*Arizono et al., 2020*) and were in accordance  
474 with the European Union and CNRS UMR5297 institutional guidelines for the care and use of lab-  
475 oratory animals (Council directive 2010/63/EU). Organotypic hippocampal slices (Gähwiler type)  
476 were dissected from 5–7-d-old wild-type mice and cultured 5–8 week in a roller drum at 35°C, as  
477 previously described (*Gähwiler, 1981*).

#### 478 **Viral infection**

479 AAV9-GFAP-GCaMP6s (*Stobart et al., 2018b*) was injected by brief pressure pulses (40ms; 15  
480 psi) into the stratum radiatum of 2-3-week old slices from Thy1-YFP-H (JAX:003782) mice 4-6 weeks  
481 prior to the experiment.

#### 482 **Image acquisition**

483 For Ca<sup>2+</sup> imaging, we used a custom-built setup based on an inverted microscope body (Leica  
484 DMI6000), as previously described in (*Tønnesen et al., 2011*). We used a 1.3 NA glycerol immersion  
485 objective equipped with a correction collar to reduce spherical aberrations and thereby allow imag-  
486 ing deeper inside brain tissue (*Urban et al., 2011*). The excitation light was provided by a pulsed  
487 diode laser ( $\lambda = 485$  nm, PicoQuant, Berlin, Germany). The fluorescence signal was confocally de-  
488 tected by an avalanche photodiode (APD; SPCM-AQRH-14-FC; PerkinElmer). The spatial resolution  
489 of the setup was around 175 nm (in x-y) and 450 nm (z). Confocal time-lapse imaging (12.5 x 25  
490  $\mu\text{m}$ , pixel size 100 nm) was performed at 2Hz for 2.5 min in artificial cerebrospinal fluid containing  
491 125 mM NaCl, 2.5 mM KCl, 1.3 mM MgCl<sub>2</sub>, 2 mM CaCl<sub>2</sub>, 26 mM NaHCO<sub>3</sub>, 1.25 mM NaH<sub>2</sub>PO<sub>4</sub>, 20 mM  
492 D-glucose, 1 mM Trolox; 300 mOsm; pH 7.4. Perfusion rate was 2 mL/min and the temperature 32

493 °C. Hypo-osmotic stress (300 mOsm to 200 mOsm) was applied by perfusing ACSF with reduced  
494 NaCl concentration (119 to 69 mM NaCl).

## 495 **Quantification and statistical analysis**

496 For each parameter set, 20 simulations, with different seeds, were generated. Each parameter  
497 describing Ca<sup>2+</sup> dynamics was expressed as mean ± standard deviation. The effect of  $d_{\text{shaft}}$  on each  
498 Ca<sup>2+</sup> signal characteristic was tested using one-way ANOVA. Comparison between two different  
499 conditions was performed using unpaired Student T-test if values followed a Gaussian distribution,  
500 Mann-Whitney test otherwise. Significance is assigned by \* for  $p \leq 0.05$ , \*\* for  $p \leq 0.01$ , \*\*\* for  
501  $p \leq 0.001$ .

## 502 **Simulation code**

503 The simulation code, implemented with STEPS 3.5.0, and the meshes are available on ModelDB  
504 (*McDougal et al., 2017*) at <http://modeldb.yale.edu/266928>, access code: Ito42@tpk3D?. The origi-  
505 nal model from Denizot et al. (*Denizot et al., 2019a*) is available at <http://modeldb.yale.edu/247694>.

## 506 **Acknowledgments**

507 This work was funded by the Okinawa Institute of Science and Technology Graduate University  
508 and by JSPS (Japan Society for the Promotion of Science) Postdoctoral Fellowship for Research in  
509 Japan (Standard, P21733). We thank Iain Hepburn and Weiliang Chen of the Computational Neuro-  
510 science Unit, OIST, Okinawa, Japan for discussion about 3D meshes and STEPS.

## 511 **References**

- 512 **Aboufares El Alaoui A**, Jackson M, Fabri M, de Vivo L, Bellesi M. Characterization of Subcellular Organelles in  
513 Cortical Perisynaptic Astrocytes. *Frontiers in Cellular Neuroscience*. 2021; 14. [https://www.frontiersin.org/](https://www.frontiersin.org/articles/10.3389/fncel.2020.573944/full)  
514 [articles/10.3389/fncel.2020.573944/full](https://www.frontiersin.org/articles/10.3389/fncel.2020.573944/full), doi: 10.3389/fncel.2020.573944, publisher: Frontiers.
- 515 **Agarwal A**, Wu PH, Hughes EG, Fukaya M, Tischfield MA, Langseth AJ, Wirtz D, Bergles DE. Transient Opening  
516 of the Mitochondrial Permeability Transition Pore Induces Microdomain Calcium Transients in Astrocyte Pro-  
517 cesses. *Neuron*. 2017 Feb; 93(3):587–605.e7. [http://www.cell.com/neuron/abstract/S0896-6273\(16\)31007-8](http://www.cell.com/neuron/abstract/S0896-6273(16)31007-8),  
518 doi: 10.1016/j.neuron.2016.12.034.
- 519 **Ahmadpour N**, Kantroo M, Stobart JL. Extracellular Calcium Influx Pathways in Astrocyte Calcium Microdomain  
520 Physiology. *Biomolecules*. 2021 Oct; 11(10):1467. <https://www.mdpi.com/2218-273X/11/10/1467>, doi:  
521 10.3390/biom11101467, number: 10 Publisher: Multidisciplinary Digital Publishing Institute.
- 522 **Araya R**, Vogels TP, Yuste R. Activity-dependent dendritic spine neck changes are correlated with synaptic  
523 strength. *Proceedings of the National Academy of Sciences*. 2014 Jul; 111(28):E2895–E2904. [https://www.](https://www.pnas.org/content/111/28/E2895)  
524 [pnas.org/content/111/28/E2895](https://www.pnas.org/content/111/28/E2895), doi: 10.1073/pnas.1321869111, publisher: National Academy of Sciences  
525 Section: PNAS Plus.
- 526 **Arizono M**, Bancelin S, Bethge P, Chéreau R, Idziak A, Inavalli VVGK, Pfeiffer T, Tønnesen J, Nägerl UV. Nanoscale  
527 imaging of the functional anatomy of the brain. *Neuroforum*. 2021 Mar; [https://www.degruyter.com/](https://www.degruyter.com/document/doi/10.1515/nf-2021-0004/html)  
528 [document/doi/10.1515/nf-2021-0004/html](https://www.degruyter.com/document/doi/10.1515/nf-2021-0004/html), doi: 10.1515/nf-2021-0004, publisher: De Gruyter Section: Neuro-  
529 forum.
- 530 **Arizono M**, Inavalli VVGK, Bancelin S, Fernández-Monreal M, Nägerl UV. Super-resolution shadow imag-  
531 ing reveals local remodeling of astrocytic microstructures and brain extracellular space after osmotic  
532 challenge. *Glia*. 2021; 69(6):1605–1613. <https://onlinelibrary.wiley.com/doi/abs/10.1002/glia.23995>, doi:  
533 [10.1002/glia.23995](https://onlinelibrary.wiley.com/doi/abs/10.1002/glia.23995), eprint: <https://onlinelibrary.wiley.com/doi/pdf/10.1002/glia.23995>.
- 534 **Arizono M**, Inavalli VVGK, Panatier A, Pfeiffer T, Angibaud J, Lvet F, Veer MJTT, Stobart J, Bellocchio L,  
535 Mikoshiba K, Marsicano G, Weber B, Olier SHR, Nägerl UV. Structural basis of astrocytic Ca<sup>2+</sup> signals  
536 at tripartite synapses. *Nature Communications*. 2020 Apr; 11(1):1–15. [https://www.nature.com/articles/](https://www.nature.com/articles/s41467-020-15648-4)  
537 [s41467-020-15648-4](https://www.nature.com/articles/s41467-020-15648-4), doi: 10.1038/s41467-020-15648-4, number: 1 Publisher: Nature Publishing Group.
- 538 **Arizono M**, Nägerl UV. Deciphering the functional nano-anatomy of the tripartite synapse using simulated  
539 emission depletion microscopy. *Glia*. 2021; n/a(n/a). [https://onlinelibrary.wiley.com/doi/abs/10.1002/glia.](https://onlinelibrary.wiley.com/doi/abs/10.1002/glia.24103)  
540 [24103](https://onlinelibrary.wiley.com/doi/abs/10.1002/glia.24103), doi: 10.1002/glia.24103, eprint: <https://onlinelibrary.wiley.com/doi/pdf/10.1002/glia.24103>.

- 541 **Bartol TM**, Keller DX, Kinney JP, Bajaj CL, Harris KM, Sejnowski TJ, Kennedy MB. Computational reconstitution  
542 of spine calcium transients from individual proteins. *Frontiers in Synaptic Neuroscience*. 2015 Oct; 7. <https://www.ncbi.nlm.nih.gov/pmc/articles/PMC4595661/>, doi: 10.3389/fnsyn.2015.00017.
- 544 **Bell M**, Bartol T, Sejnowski T, Rangamani P. Dendritic spine geometry and spine apparatus organization govern  
545 the spatiotemporal dynamics of calcium. *The Journal of General Physiology*. 2019 Aug; 151(8):1017–1034.  
546 <http://jgp.rupress.org/content/151/8/1017>, doi: 10.1085/jgp.201812261.
- 547 **Bezprozvanny I**, Watras J, Ehrlich BE. Bell-shaped calcium-response curves of Ins(1,4,5)P<sub>3</sub>- and calcium-  
548 gated channels from endoplasmic reticulum of cerebellum. *Nature*. 1991 Jun; 351(6329):751–754. doi:  
549 10.1038/351751a0.
- 550 **Biess A**, Korkotian E, Holcman D. Diffusion in a dendritic spine: The role of geometry. *Physical Review E*. 2007  
551 Aug; 76(2):021922. <https://link.aps.org/doi/10.1103/PhysRevE.76.021922>, doi: 10.1103/PhysRevE.76.021922,  
552 publisher: American Physical Society.
- 553 **Bindocci E**, Savtchouk I, Liaudet N, Becker D, Carriero G, Volterra A. Three-dimensional Ca<sup>2+</sup> imaging advances  
554 understanding of astrocyte biology. *Science*. 2017 May; 356(6339):eaai8185. [http://science.sciencemag.org/  
555 content/356/6339/eaai8185](http://science.sciencemag.org/content/356/6339/eaai8185), doi: 10.1126/science.aai8185.
- 556 **Brazhe AR**, Postnov DE, Sosnovtseva O. Astrocyte calcium signaling: Interplay between structural and dyn-  
557 amical patterns. *Chaos: An Interdisciplinary Journal of Nonlinear Science*. 2018 Oct; 28(10):106320. [https://  
558 /aip.scitation.org/doi/abs/10.1063/1.5037153](https://aip.scitation.org/doi/abs/10.1063/1.5037153), doi: 10.1063/1.5037153.
- 559 **Bushong EA**, Martone ME, Jones YZ, Ellisman MH. Protoplasmic astrocytes in CA1 stratum radiatum occupy sep-  
560 arate anatomical domains. *The Journal of Neuroscience: The Official Journal of the Society for Neuroscience*.  
561 2002 Jan; 22(1):183–192.
- 562 **Cali C**, Agus M, Kare K, Boges DJ, Lehvaslaiho H, Hadwiger M, Magistretti PJ. 3D cellular reconstruction of  
563 cortical glia and parenchymal morphometric analysis from Serial Block-Face Electron Microscopy of juve-  
564 nile rat. *Progress in Neurobiology*. 2019 Sep; p. 101696. [http://www.sciencedirect.com/science/article/pii/  
565 S0301008219300139](http://www.sciencedirect.com/science/article/pii/S0301008219300139), doi: 10.1016/j.pneurobio.2019.101696.
- 566 **Cugno A**, Bartol TM, Sejnowski TJ, Iyengar R, Rangamani P. Geometric principles of second messenger  
567 dynamics in dendritic spines. *Scientific Reports*. 2019 Aug; 9(1):1–18. [https://www.nature.com/articles/  
568 s41598-019-48028-0](https://www.nature.com/articles/s41598-019-48028-0), doi: 10.1038/s41598-019-48028-0, number: 1 Publisher: Nature Publishing Group.
- 569 **De Young GW**, Keizer J. A single-pool inositol 1,4,5-trisphosphate-receptor-based model for agonist-stimulated  
570 oscillations in Ca<sup>2+</sup> concentration. *Proceedings of the National Academy of Sciences*. 1992 Oct; 89(20):9895–  
571 9899. <http://www.pnas.org/cgi/doi/10.1073/pnas.89.20.9895>, doi: 10.1073/pnas.89.20.9895.
- 572 **Denizot A**, Arizono M, Nägerl UV, Soula H, Berry H. Simulation of calcium signaling in fine astrocytic  
573 processes: Effect of spatial properties on spontaneous activity. *PLOS Computational Biology*. 2019  
574 Aug; 15(8):e1006795. <https://journals.plos.org/ploscompbiol/article?id=10.1371/journal.pcbi.1006795>, doi:  
575 10.1371/journal.pcbi.1006795.
- 576 **Denizot A**, Berry H, Venugopal S. Computational Modeling of Intracellular Ca<sup>2+</sup> Signals in Astrocytes. *Encyclo-  
577 pedia of Computational Neuroscience*. 2019; p. Submitted. Submitted.
- 578 **Di Castro MA**, Chuquet J, Liaudet N, Bhaukaurally K, Santello M, Bouvier D, Tiret P, Volterra A. Local Ca<sup>2+</sup>  
579 detection and modulation of synaptic release by astrocytes. *Nature Neuroscience*. 2011 Oct; 14(10):1276–  
580 1284. doi: 10.1038/nn.2929.
- 581 **Giaume C**, Venance L. Intercellular calcium signaling and gap junctional communication in astrocytes. *Glia*.  
582 1998 Sep; 24(1):50–64. [http://onlinelibrary.wiley.com/insb.bib.cnrs.fr/doi/10.1002/\(SICI\)1098-1136\(199809\)24:  
583 1<50::AID-GLIA6>3.0.CO;2-4/abstract](http://onlinelibrary.wiley.com/insb.bib.cnrs.fr/doi/10.1002/(SICI)1098-1136(199809)24:1<50::AID-GLIA6>3.0.CO;2-4/abstract), doi: 10.1002/(SICI)1098-1136(199809)24:1<50::AID-GLIA6>3.0.CO;2-  
584 4.
- 585 **Gillespie DT**. Exact stochastic simulation of coupled chemical reactions. *The Journal of Physical Chemistry*.  
586 1977 Dec; 81(25):2340–2361. <https://doi.org/10.1021/j100540a008>, doi: 10.1021/j100540a008.
- 587 **Grosche J**, Matyash V, Möller T, Verkhratsky A, Reichenbach A, Kettenmann H. Microdomains for neuron–glia  
588 interaction: parallel fiber signaling to Bergmann glial cells. *Nature Neuroscience*. 1999 Feb; 2(2):139–143.  
589 [https://www.nature.com/articles/nn0299\\_139](https://www.nature.com/articles/nn0299_139), doi: 10.1038/5692.

- 590 **Gähwiler BH.** Organotypic monolayer cultures of nervous tissue. *Journal of Neuroscience Methods*. 1981  
591 Dec; 4(4):329–342. <http://www.sciencedirect.com/science/article/pii/0165027081900030>, doi: 10.1016/0165-  
592 0270(81)90003-0.
- 593 **Haustein MD,** Kracun S, Lu XH, Shih T, Jackson-Weaver O, Tong X, Xu J, Yang XW, O'Dell TJ, Marvin JS, Ellisman  
594 MH, Bushong EA, Looger LL, Khakh BS. Conditions and constraints for astrocyte calcium signaling in the  
595 hippocampal mossy fiber pathway. *Neuron*. 2014 Apr; 82(2):413–429. doi: 10.1016/j.neuron.2014.02.041.
- 596 **Henneberger C,** Bard L, Panatier A, Reynolds JP, Kopach O, Medvedev NI, Minge D, Herde MK, Anders S, Kraev  
597 I, Heller JP, Rama S, Zheng K, Jensen TP, Sanchez-Romero I, Jackson CJ, Janovjak H, Ottersen OP, Nagel-  
598 hus EA, Oliet SHR, et al. LTP Induction Boosts Glutamate Spillover by Driving Withdrawal of Perisynap-  
599 tic Astroglia. *Neuron*. 2020 Sep; <http://www.sciencedirect.com/science/article/pii/S0896627320306619>, doi:  
600 10.1016/j.neuron.2020.08.030.
- 601 **Hepburn I,** Chen W, Wils S, De Schutter E. STEPS: efficient simulation of stochastic reaction–diffusion models  
602 in realistic morphologies. *BMC Systems Biology*. 2012; 6(1):36. [http://bmcsystbiol.biomedcentral.com/articles/](http://bmcsystbiol.biomedcentral.com/articles/10.1186/1752-0509-6-36)  
603 [10.1186/1752-0509-6-36](http://doi.org/10.1186/1752-0509-6-36), doi: 10.1186/1752-0509-6-36.
- 604 **Holbro N,** Grunditz A, Oertner TG. Differential distribution of endoplasmic reticulum controls metabotropic  
605 signaling and plasticity at hippocampal synapses. *Proceedings of the National Academy of Sciences*. 2009  
606 Sep; 106(35):15055–15060. <https://www.pnas.org/content/106/35/15055>, doi: 10.1073/pnas.0905110106,  
607 publisher: National Academy of Sciences Section: Biological Sciences.
- 608 **Holcman D,** Schuss Z. Modeling Calcium Dynamics in Dendritic Spines. *SIAM Journal on Applied Math-*  
609 *ematics*. 2005 Jan; 65(3):1006–1026. <https://epubs.siam.org/doi/abs/10.1137/S003613990342894X>, doi:  
610 10.1137/S003613990342894X.
- 611 **Holcman D,** Schuss Z. Diffusion laws in dendritic spines. *The Journal of Mathematical Neuroscience*. 2011 Oct;  
612 1(1):10. <https://doi.org/10.1186/2190-8567-1-10>, doi: 10.1186/2190-8567-1-10.
- 613 **Isaacson SA,** Isaacson D. The Reaction-Diffusion Master Equation, Diffusion Limited Reactions, and Singular  
614 Potentials. *Physical Review E, Statistical, Nonlinear, and Soft Matter Physics*. 2009 Dec; 80(6 Pt 2):066106.  
615 <http://www.ncbi.nlm.nih.gov/pmc/articles/PMC3405976/>.
- 616 **Kiyoshi CM,** Aten S, Arzola EP, Patterson JA, Taylor AT, Du Y, Guiher AM, Philip M, Camacho EG, Mediratta D,  
617 Collins K, Benson E, Kidd G, Terman D, Zhou M. Ultrastructural view of astrocyte-astrocyte and astrocyte-  
618 synapse contacts within the hippocampus; 2020.
- 619 **Kucharz K,** Wieloch T, Toresson H. Fission and Fusion of the Neuronal Endoplasmic Reticulum. *Translational*  
620 *Stroke Research*. 2013 Dec; 4(6):652–662. <https://link.springer.com/article/10.1007/s12975-013-0279-9>, doi:  
621 10.1007/s12975-013-0279-9.
- 622 **Lafrenaye AD,** Simard JM. Bursting at the Seams: Molecular Mechanisms Mediating Astrocyte Swelling. *Inter-*  
623 *national Journal of Molecular Sciences*. 2019 Jan; 20(2):330. <https://www.mdpi.com/1422-0067/20/2/330>, doi:  
624 10.3390/ijms20020330, number: 2 Publisher: Multidisciplinary Digital Publishing Institute.
- 625 **Lind BL,** Brazhe AR, Jessen SB, Tan FCC, Lauritzen MJ. Rapid stimulus-evoked astrocyte Ca<sup>2+</sup> elevations and  
626 hemodynamic responses in mouse somatosensory cortex in vivo. *Proceedings of the National Academy*  
627 *of Sciences*. 2013 Nov; p. 201310065. <http://www.pnas.org/content/early/2013/11/08/1310065110>, doi:  
628 10.1073/pnas.1310065110.
- 629 **Majewska A,** Brown E, Ross J, Yuste R. Mechanisms of Calcium Decay Kinetics in Hippocampal Spines: Role  
630 of Spine Calcium Pumps and Calcium Diffusion through the Spine Neck in Biochemical Compartmentaliza-  
631 tion. *Journal of Neuroscience*. 2000 Mar; 20(5):1722–1734. <http://www.jneurosci.org/content/20/5/1722>, doi:  
632 10.1523/JNEUROSCI.20-05-01722.2000.
- 633 **McDougal RA,** Morse TM, Carnevale T, Marengo L, Wang R, Migliore M, Miller PL, Shepherd GM, Hines ML.  
634 Twenty years of ModelDB and beyond: building essential modeling tools for the future of neuroscience.  
635 *Journal of Computational Neuroscience*. 2017 Feb; 42(1):1–10. doi: 10.1007/s10827-016-0623-7.
- 636 **Noguchi J,** Matsuzaki M, Ellis-Davies GCR, Kasai H. Spine-Neck Geometry Determines NMDA Receptor-  
637 Dependent Ca<sup>2+</sup> Signaling in Dendrites. *Neuron*. 2005 May; 46(4):609–622. [http://www.sciencedirect.com/](http://www.sciencedirect.com/science/article/pii/S0896627305002382)  
638 [science/article/pii/S0896627305002382](http://doi.org/10.1016/j.neuron.2005.03.015), doi: 10.1016/j.neuron.2005.03.015.
- 639 **Oberheim NA,** Wang X, Goldman S, Nedergaard M. Astrocytic complexity distinguishes the human brain.  
640 *Trends in Neurosciences*. 2006 Oct; 29(10):547–553. doi: 10.1016/j.tins.2006.08.004.

- 641 **Otsu Y**, Couchman K, Lyons DG, Collot M, Agarwal A, Mallet JM, Pfrieger FW, Bergles DE, Charpak S. Calcium  
642 dynamics in astrocyte processes during neurovascular coupling. *Nature Neuroscience*. 2015 Feb; 18(2):210-  
643 218. <http://www.nature.com/neuro/journal/v18/n2/full/nn.3906.html>, doi: 10.1038/nn.3906.
- 644 **Panatier A**, Arizono M, Nägerl UV. Dissecting tripartite synapses with STED microscopy. *Phil Trans R Soc*  
645 *B*. 2014 Oct; 369(1654):20130597. <http://rstb.royalsocietypublishing.org/content/369/1654/20130597>, doi:  
646 10.1098/rstb.2013.0597.
- 647 **Panatier A**, Vallée J, Haber M, Murai KK, Lacaille JC, Robitaille R. Astrocytes are endogenous regulators of basal  
648 transmission at central synapses. *Cell*. 2011 Sep; 146(5):785–798. doi: 10.1016/j.cell.2011.07.022.
- 649 **Poirazi P**, Papoutsi A. Illuminating dendritic function with computational models. *Nature Reviews Neuro-*  
650 *science*. 2020 Jun; 21(6):303–321. <https://www.nature.com/articles/s41583-020-0301-7>, doi: 10.1038/s41583-  
651 020-0301-7, number: 6 Publisher: Nature Publishing Group.
- 652 **Reichenbach A**, Derouiche A, Kirchhoff F. Morphology and dynamics of perisynaptic glia. *Brain Research*  
653 *Reviews*. 2010 May; 63(1-2):11–25. doi: 10.1016/j.brainresrev.2010.02.003.
- 654 **Rusakov DA**. Disentangling calcium-driven astrocyte physiology. *Nature Reviews Neuroscience*. 2015 Apr;  
655 16(4):226–233. <http://www.nature.com/nrn/journal/v16/n4/full/nrn3878.html>, doi: 10.1038/nrn3878.
- 656 **Salmon CK**, Syed TA, Kacerovsky JB, Alivodej N, Schober AL, Pratte MT, Rosen MP, Green M, Chirgwin-Dasgupta  
657 A, Vali H, Mandato CA, Siddiqi K, Murai KK. Organizing Principles of Astrocytic Nanoarchitecture in the Mouse  
658 Cerebral Cortex; 2021.
- 659 **Santamaria F**, Wils S, De Schutter E, Augustine GJ. The diffusional properties of dendrites depend on the density  
660 of dendritic spines. *The European Journal of Neuroscience*. 2011 Aug; 34(4):561–568. doi: 10.1111/j.1460-  
661 9568.2011.07785.x.
- 662 **Schmidt H**, Eilers J. Spine neck geometry determines spino-dendritic cross-talk in the presence of mobile  
663 endogenous calcium binding proteins. *Journal of Computational Neuroscience*. 2009 Oct; 27(2):229–243.  
664 <https://doi.org/10.1007/s10827-009-0139-5>, doi: 10.1007/s10827-009-0139-5.
- 665 **Schuss Z**, Singer A, Holcman D. The narrow escape problem for diffusion in cellular microdomains. *Proceedings*  
666 *of the National Academy of Sciences*. 2007 Oct; 104(41):16098–16103. [https://www.pnas.org/content/104/41/  
667 16098](https://www.pnas.org/content/104/41/16098), doi: 10.1073/pnas.0706599104, publisher: National Academy of Sciences Section: Physical Sciences.
- 668 **Semyanov A**, Henneberger C, Agarwal A. Making sense of astrocytic calcium signals — from acquisition  
669 to interpretation. *Nature Reviews Neuroscience*. 2020 Sep; p. 1–14. [https://www.nature.com/articles/  
670 s41583-020-0361-8](https://www.nature.com/articles/s41583-020-0361-8), doi: 10.1038/s41583-020-0361-8, publisher: Nature Publishing Group.
- 671 **Sherwood MW**, Arizono M, Hisatsune C, Bannai H, Ebisui E, Sherwood JL, Panatier A, Oliet SHR, Mikoshiba  
672 K. Astrocytic IP3Rs: Contribution to Ca<sup>2+</sup> signalling and hippocampal LTP. *Glia*. 2017 Mar; 65(3):502–513.  
673 <http://onlinelibrary.wiley.com/doi/10.1002/glia.23107/abstract>, doi: 10.1002/glia.23107.
- 674 **Shigetomi E**, Bushong EA, Hausteiner MD, Tong X, Jackson-Weaver O, Kracun S, Xu J, Sofroniew MV, Ellisman  
675 MH, Khakh BS. Imaging calcium microdomains within entire astrocyte territories and endfeet with GCaMPs  
676 expressed using adeno-associated viruses. *The Journal of General Physiology*. 2013 May; 141(5):633–647.  
677 doi: 10.1085/jgp.201210949.
- 678 **Shigetomi E**, Patel S, Khakh BS. Probing the Complexities of Astrocyte Calcium Signaling. *Trends in Cell Biology*.  
679 2016 Apr; 26(4):300–312. doi: 10.1016/j.tcb.2016.01.003.
- 680 **Shigetomi E**, Saito K, Sano F, Koizumi S. Aberrant Calcium Signals in Reactive Astrocytes: A Key Process in  
681 Neurological Disorders. *International Journal of Molecular Sciences*. 2019 Jan; 20(4):996. [https://www.mdpi.  
682 com/1422-0067/20/4/996](https://www.mdpi.com/1422-0067/20/4/996), doi: 10.3390/ijms20040996.
- 683 **Simon CM**, Hepburn I, Chen W, Schutter ED. The role of dendritic spine morphology in the compartmental-  
684 ization and delivery of surface receptors. *Journal of Computational Neuroscience*. 2014 Jun; 36(3):483–497.  
685 <https://link.springer.com/article/10.1007/s10827-013-0482-4>, doi: 10.1007/s10827-013-0482-4.
- 686 **Smith S**, Grima R. Spatial Stochastic Intracellular Kinetics: A Review of Modelling Approaches. *Bulletin of*  
687 *Mathematical Biology*. 2018 May; <https://doi.org/10.1007/s11538-018-0443-1>, doi: 10.1007/s11538-018-0443-  
688 1.

- 689 **Spacek J**, Harris KM. Three-Dimensional Organization of Smooth Endoplasmic Reticulum in Hippocampal  
690 CA1 Dendrites and Dendritic Spines of the Immature and Mature Rat. *Journal of Neuroscience*. 1997 Jan;  
691 17(1):190–203. <http://www.jneurosci.org/content/17/1/190>, doi: 10.1523/JNEUROSCI.17-01-00190.1997.
- 692 **Srinivasan R**, Huang BS, Venugopal S, Johnston AD, Chai H, Zeng H, Golshani P, Khakh BS. Ca<sup>2+</sup> signaling  
693 in astrocytes from *Ip3r2(-/-)* mice in brain slices and during startle responses in vivo. *Nature Neuroscience*.  
694 2015 May; 18(5):708–717. doi: 10.1038/nn.4001.
- 695 **Stobart JL**, Ferrari KD, Barrett MJP, Glück C, Stobart MJ, Zuend M, Weber B. Cortical Circuit Activity Evokes  
696 Rapid Astrocyte Calcium Signals on a Similar Timescale to Neurons. *Neuron*. 2018 May; 98(4):726–735.e4.  
697 <http://www.sciencedirect.com/science/article/pii/S0896627318302848>, doi: 10.1016/j.neuron.2018.03.050.
- 698 **Stobart JL**, Ferrari KD, Barrett MJP, Stobart MJ, Looser ZJ, Saab AS, Weber B. Long-term In Vivo Calcium Imaging  
699 of Astrocytes Reveals Distinct Cellular Compartment Responses to Sensory Stimulation. *Cerebral Cortex*  
700 (New York, NY: 1991). 2018 Jan; 28(1):184–198. doi: 10.1093/cercor/bhw366.
- 701 **Theodosis DT**, Poulain DA, Oliet SHR. Activity-dependent structural and functional plasticity of astrocyte-  
702 neuron interactions. *Physiological Reviews*. 2008 Jul; 88(3):983–1008. doi: 10.1152/physrev.00036.2007.
- 703 **Tønnesen J**, Katona G, Rózsa B, Nägerl UV. Spine neck plasticity regulates compartmentalization of  
704 synapses. *Nature Neuroscience*. 2014 May; 17(5):678–685. <https://www.nature.com/articles/nn.3682>, doi:  
705 10.1038/nn.3682, number: 5 Publisher: Nature Publishing Group.
- 706 **Tønnesen J**, Nadrigny F, Willig K, Wedlich-Söldner R, Nägerl UV. Two-Color STED Microscopy of Living Synapses  
707 Using A Single Laser-Beam Pair. *Biophysical Journal*. 2011 Nov; 101(10):2545–2552. <http://www.sciencedirect.com/science/article/pii/S0006349511012008>, doi: 10.1016/j.bpj.2011.10.011.
- 708
- 709 **Urban N**, Willig K, Hell S, Nägerl UV. STED Nanoscopy of Actin Dynamics in Synapses Deep Inside Living Brain  
710 Slices. *Biophysical Journal*. 2011 Sep; 101(5):1277–1284. <http://www.sciencedirect.com/science/article/pii/S000634951100885X>, doi: 10.1016/j.bpj.2011.07.027.
- 711
- 712 **Verkhatsky A**, Nedergaard M. Physiology of Astroglia. *Physiological Reviews*. 2018 Jan; 98(1):239–389. doi:  
713 10.1152/physrev.00042.2016.
- 714 **Witcher MR**, Kirov SA, Harris KM. Plasticity of perisynaptic astroglia during synaptogenesis in the mature rat  
715 hippocampus. *Glia*. 2007 Jan; 55(1):13–23. doi: 10.1002/glia.20415.
- 716 **Wu YW**, Gordleeva S, Tang X, Shih PY, Dembitskaya Y, Semyanov A. Morphological profile determines the  
717 frequency of spontaneous calcium events in astrocytic processes. *bioRxiv*. 2018 Sep; p. 410076. [https://](https://www.biorxiv.org/content/early/2018/09/06/410076)  
718 [www.biorxiv.org/content/early/2018/09/06/410076](https://www.biorxiv.org/content/early/2018/09/06/410076), doi: 10.1101/410076.
- 719 **Wybo WAM**, Torben-Nielsen B, Nevian T, Gewaltig MO. Electrical Compartmentalization in Neurons. *Cell Re-*  
720 *ports*. 2019 Feb; 26(7):1759–1773.e7. <https://www.sciencedirect.com/science/article/pii/S2211124719301032>,  
721 doi: 10.1016/j.celrep.2019.01.074.
- 722 **Yasuda R**. Biophysics of Biochemical Signaling in Dendritic Spines: Implications in Synaptic Plastic-  
723 ity. *Biophysical Journal*. 2017 Nov; 113(10):2152–2159. <http://www.sciencedirect.com/science/article/pii/S000634951730855X>, doi: 10.1016/j.bpj.2017.07.029.
- 724
- 725 **Yuste R**, Majewska A, Holthoff K. From form to function: calcium compartmentalization in dendritic spines.  
726 *Nature Neuroscience*. 2000 Jul; 3(7):653–659. doi: 10.1038/76609.
- 727 **Zhou B**, Zuo YX, Jiang RT. Astrocyte morphology: Diversity, plasticity, and role in neurological diseases. *CNS*  
728 *neuroscience & therapeutics*. 2019 Mar; doi: 10.1111/cns.13123.

**Table 2. Characteristics of meshes used to investigate the effect of voxel size on  $\text{Ca}^{2+}$  signals.** Cylinder geometries were generated with various total number of tetrahedra (geometry  $Cyl_i$  with  $i \in [1, 8]$ , see also Fig 1A), resulting in different voxel sizes.  $V_{\text{mean}}$  corresponds to the average voxel volume,  $V_{\text{std}}$  to its standard deviation,  $V_{\text{max}}$  to the maximum voxel volume and  $V_{\text{min}}$  to the minimum voxel volume in the mesh. Volumes are expressed in  $\text{nm}^3$ . Diff ( $\text{nm}^3$ ) corresponds to  $V_{\text{max}} - V_{\text{min}}$  while Diff (%) is the ratio  $\frac{V_{\text{max}} - V_{\text{min}}}{V_{\text{mean}}} * 100$

Geom	# tet	$V_{\text{mean}}$	$V_{\text{std}}$	$V_{\text{max}}$	$V_{\text{min}}$	Diff ( $\text{nm}^3$ )	Diff (%)
$Cyl_1$	372148	84	25	296	15	281	335
$Cyl_2$	274233	115	34	389	20	369	321
$Cyl_3$	125927	249	71	761	33	728	292
$Cyl_4$	40077	782	229	2200	67	2133	273
$Cyl_5$	11523	2700	790	7521	177	7344	272
$Cyl_6$	3103	9900	3200	24000	94	23906	241
$Cyl_7$	1417	21000	11000	62000	241	61759	294
$Cyl_8$	945	32000	28000	145000	241	144759	452

### 729 **Supplemental Movie 1**

730 Movie presenting a simulation of the bleaching protocol, with  $d_{\text{shaft}} = \frac{d_0}{2}$ . Fluorescing ZsGreen  
731 molecules are in red and bleached, non-fluorescing, ZsGreen are in yellow. Molecule position  
732 was updated every 1 ms. The plot presents the variation of the number of fluorescing ZsGreen  
733 molecules with time in the central node. Note that, to facilitate visualization, here  $[\text{ZsGreen}] = 5$   
734  $\mu\text{M}$ . Before the bleaching event, all ZsGreen proteins (red) fluoresce. At bleaching time, fluorescing  
735 molecules in the bleached region encounter conformational modifications that prevent them from  
736 fluorescing (yellow molecules). Consequently, the fluorescence level drops to  $I_0$ . Because of the  
737 diffusion of molecules in the cell, the fluorescence level in the central node then increases until it  
738 reaches a new baseline  $I_{\text{inf}}$ , after a recovery time  $\tau$ . Fluorescing ZsGreen molecules are in red and  
739 bleached, non-fluorescing, ZsGreen are in yellow.

### 740 **Supplemental Movie 2**

741 Movie presenting a simulation of the neuronal stimulation protocol, with  $d_{\text{shaft}} = \frac{d_0}{2}$  and  $\text{Ca}^{2+}$  influx  
742 rate at the plasma membrane  $k_{\text{Ca}} = 0 \text{ s}^{-1}$ . 100  $\text{IP}_3$  molecules are injected in Node 1 at  $t_0 = 0.1 \text{ s}$ , while  
743 the number of Ca-GCaMP,  $\text{IP}_3$  and  $\text{IP}_3\text{R}$  channels in the open state are monitored in nodes 1 and  
744 2. Molecule position was updated every 0.1 ms. Ca-GCaMP molecules are in yellow,  $\text{IP}_3$  in red and  
745  $\text{IP}_3\text{R}$  in blue. Note that the size of molecules in the movie was increased to facilitate visualization.  
746 Speed was increased 5-fold for visualization purposes.

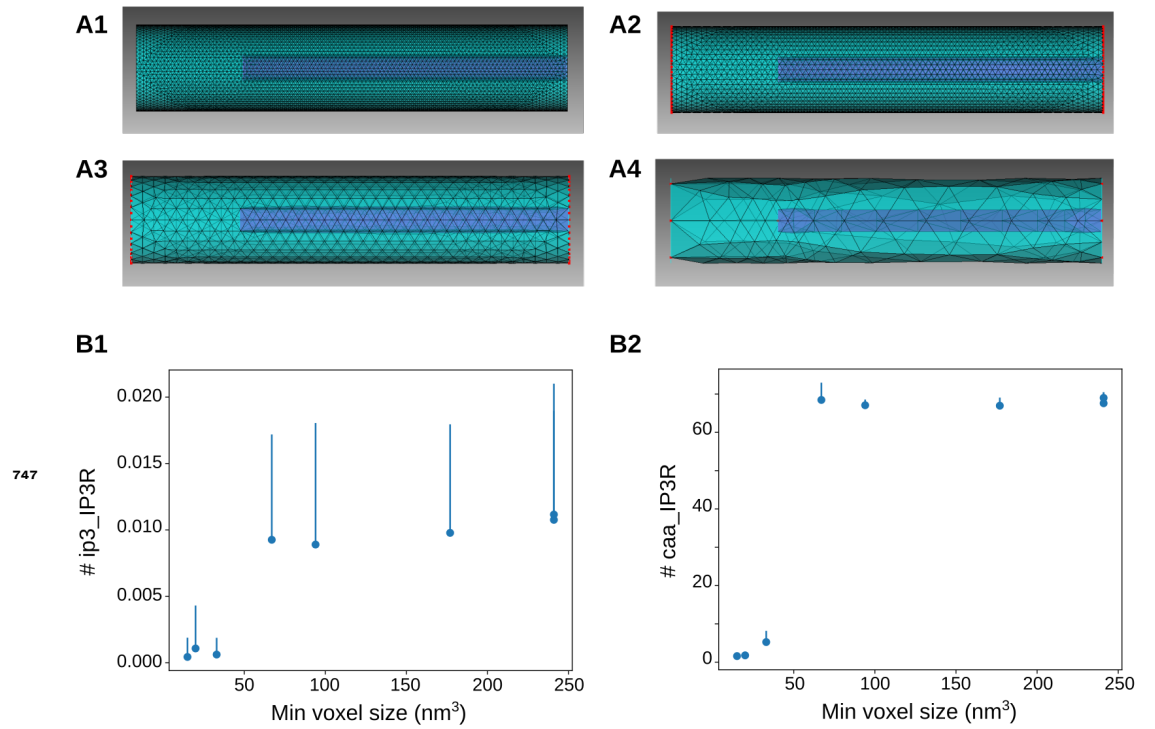


**Figure 1-Figure supplement 1. Sensitivity study of the effect of voxel size on  $\text{Ca}^{2+}$  signals.** (A) Simulations were performed in a cylinder geometry with various numbers of tetrahedra. 4 examples are presented here, "*Cyl<sub>1</sub>*" (A1), "*Cyl<sub>3</sub>*" (A2), "*Cyl<sub>5</sub>*" (A3) and "*Cyl<sub>8</sub>*" (A4). Please refer to Table 2 for details on the characteristics of each mesh. (B) Study of the average number of IP<sub>3</sub>R in the ip3\_IP3R state (IP<sub>3</sub> bound to its binding site on IP<sub>3</sub>R, B1) and in the caa\_IP3R state ( $\text{Ca}^{2+}$  bound to the activating site of IP<sub>3</sub>R, B2) depending on the minimum voxel size of the mesh.

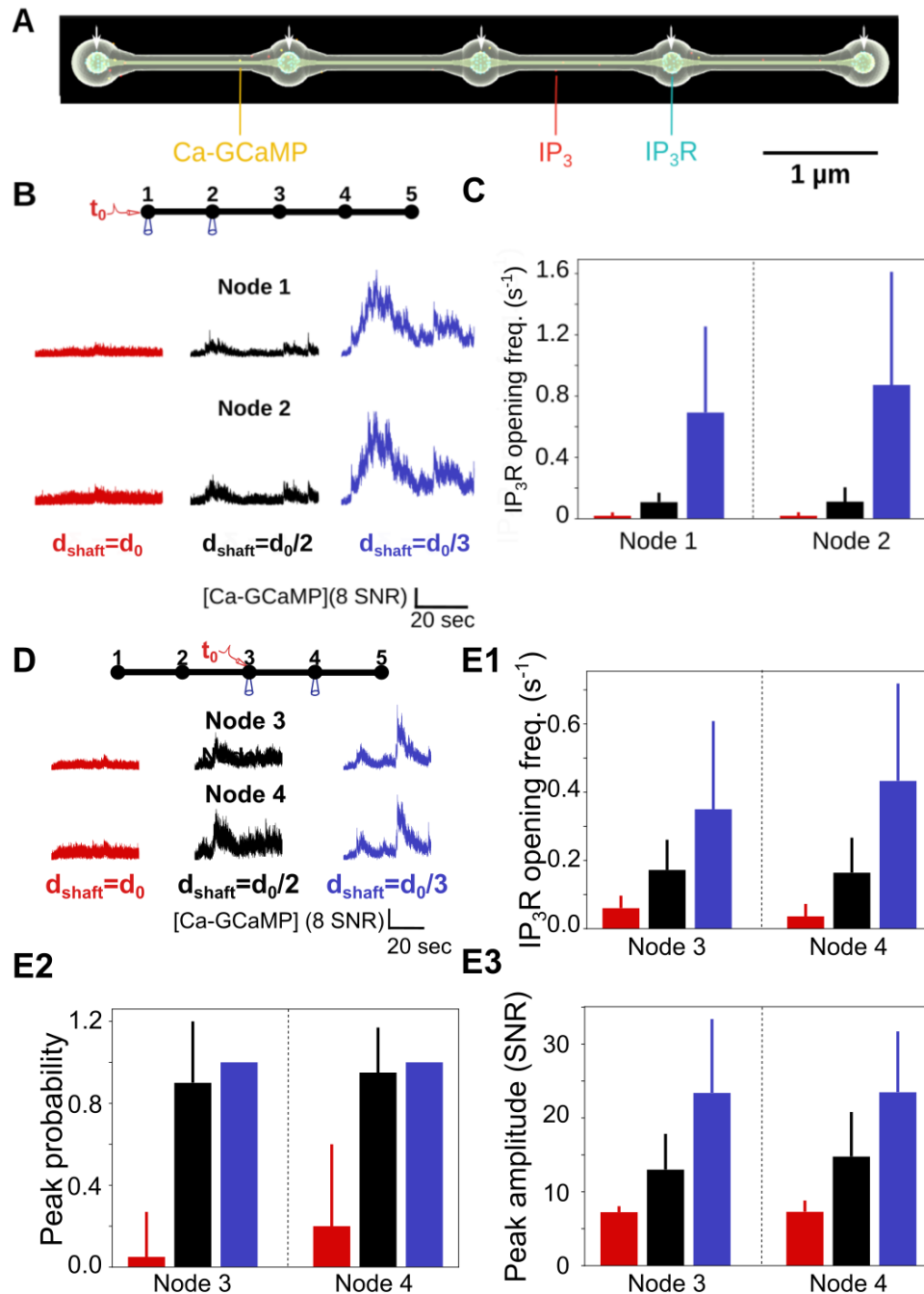


**Figure 3-Figure supplement 1. Sensitivity study of the effect of shaft width on local  $\text{Ca}^{2+}$  signals upon single node stimulation.** (A) Screenshot of a simulation in the "5nodes"  $d_{\text{shaft}} = \frac{d_0}{3}$  geometry. In those simulations,  $\text{IP}_3\text{Rs}$  are only positioned on the ER membrane in nodes (white arrows). The number of  $\text{IP}_3\text{R}$  channels is 300 for all values of  $d_{\text{shaft}}$ . (B) (Top) Node 1 was stimulated at  $t=t_0=1\text{s}$ , while  $\text{Ca}^{2+}$  activity was monitored in nodes 1 and 2. (Bottom) Representative  $\text{Ca}^{2+}$  traces in node 1 and node 2 for  $d_{\text{shaft}}=d_0$  (red),  $\frac{d_0}{2}$  (black) and  $\frac{d_0}{3}$  (blue). (C) The frequency of  $\text{IP}_3\text{R}$  opening increases with  $d_{\text{shaft}}$  decreases in nodes 1 (\*\*\*) and 2 (\*\*\*) . (D) (Top) In a second set of simulations, node 3 was stimulated at  $t=t_0=1\text{s}$  ( $k_{\text{Ca}}=0 \text{ s}^{-1}$ ), while  $\text{Ca}^{2+}$  activity was monitored in nodes 3 and 4. (Bottom) Representative  $[\text{Ca-GCaMP}]$  traces in nodes 3 and 4, expressed as SNR (see Methods), for  $d_{\text{shaft}}=d_0$  (red),  $\frac{d_0}{2}$  (black) and  $\frac{d_0}{3}$  (blue). (E1) The frequency of  $\text{IP}_3\text{R}$  opening increases when  $d_{\text{shaft}}$  decreases in node 3 (\*\*\*) and 4 (\*\*\*) . (E2)  $\text{Ca}^{2+}$  peak probability increases when  $d_{\text{shaft}}$  decreases in node 3 (\*\*\*) and 4 (\*\*\*) . (E3) Peak amplitude increases when  $d_{\text{shaft}}$  decreases in node 3 (\*\*\*) and 4 (\*\*\*) . Data are represented as mean  $\pm$  STD,  $n=20$  for each geometry. The effect of  $d_{\text{shaft}}$  on each  $\text{Ca}^{2+}$  signal characteristic was tested using one-way ANOVA. Significance is assigned by \* for  $p \leq 0.05$ , \*\* for  $p \leq 0.01$ , \*\*\* for  $p \leq 0.001$ .

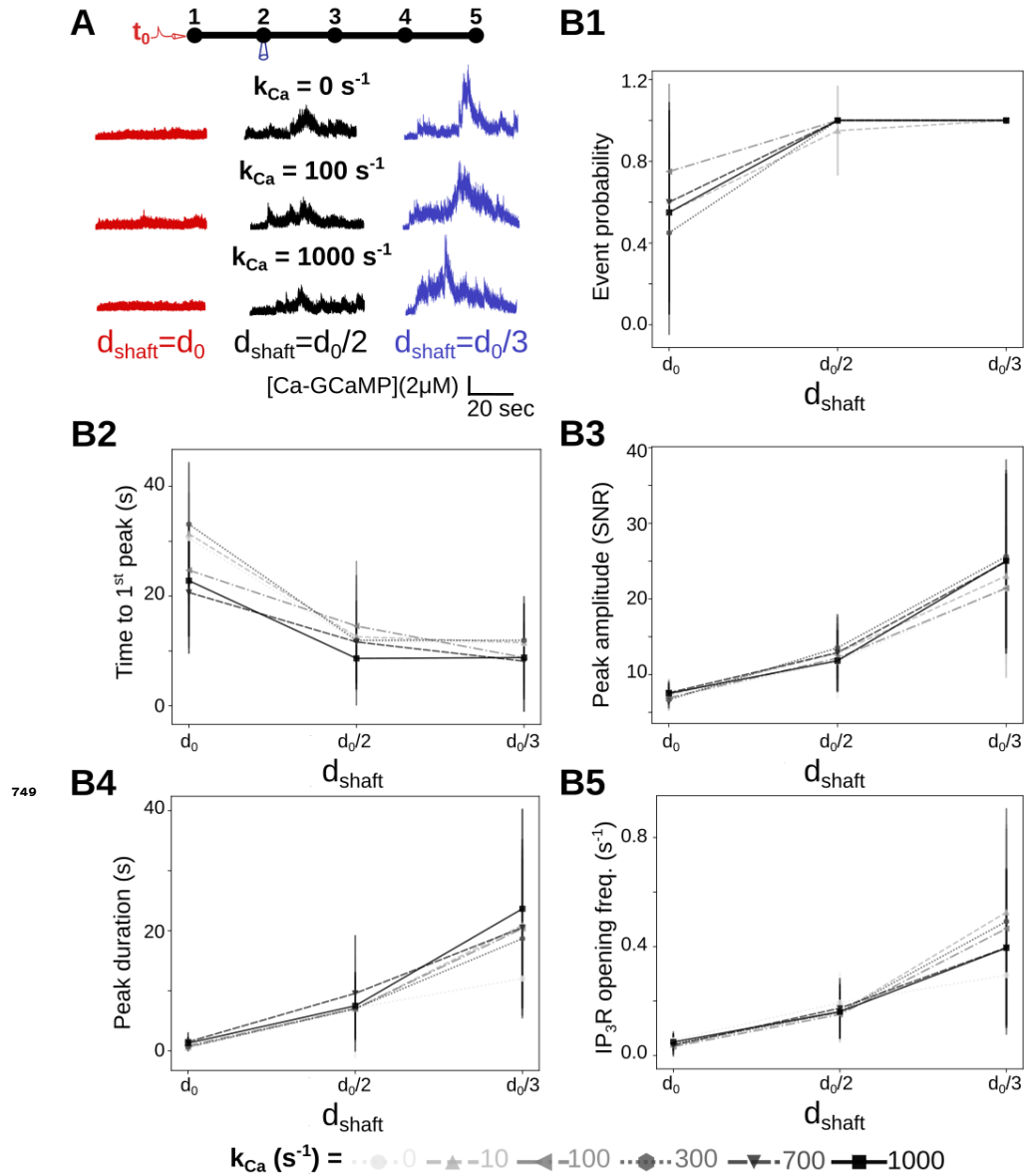
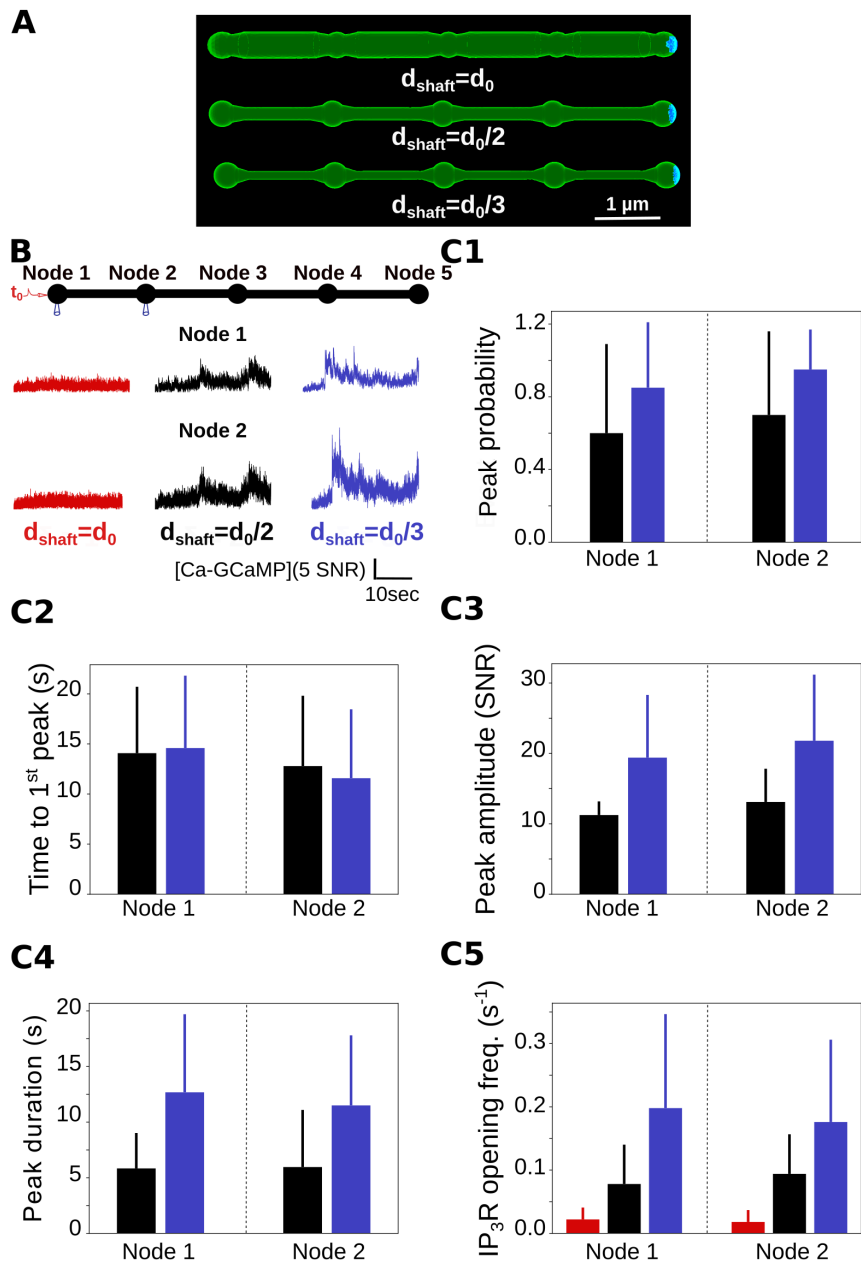


**Figure 3-Figure supplement 2. Effect of  $\text{Ca}^{2+}$  influx rate at the plasma membrane on local  $\text{Ca}^{2+}$  signals.** A) (Top) Neuronal stimulation protocol simulated for each geometry: node 1 was stimulated at  $t=t_0=1\text{s}$ , while  $\text{Ca}^{2+}$  activity was monitored in node 2. Representative  $\text{Ca}^{2+}$  traces for shaft width  $d_{\text{shaft}} = d_0$  (red),  $\frac{d_0}{2}$  (black) and  $\frac{d_0}{3}$  (blue), with a  $\text{Ca}^{2+}$  influx rate at the plasma membrane  $k_{Ca}=0$  (top), 100 (middle) and  $1000 \text{ s}^{-1}$  (bottom), expressed as SNR (see Methods). (B) Quantification of the effect of  $d_{\text{shaft}}$  on  $\text{Ca}^{2+}$  signal characteristics for  $k_{Ca}=0, 10, 100, 300, 700$  and  $1000 \text{ s}^{-1}$ . Data are represented as mean  $\pm$  STD,  $n=20$  for each set of parameters tested.  $\text{Ca}^{2+}$  peak probability increases (\*\*\*, B1), Time to 1<sup>st</sup> peak decreases (\*\*\*, B2), peak amplitude (\*\*\*, B3) and duration (\*\*\*, B4) increase when  $d_{\text{shaft}}$  decreases, for  $k_{Ca}=0, 10, 100, 300, 700$  and  $1000 \text{ s}^{-1}$ .  $\text{Ca}^{2+}$  peak characteristics did not statistically vary with  $k_{Ca}$ . The effect of  $k_{Ca}$  on each  $\text{Ca}^{2+}$  signal characteristic was tested using one-way ANOVA.



750

**Figure 3-Figure supplement 3. Sensitivity study of the effect of boundary conditions on local  $\text{Ca}^{2+}$  activity upon single node stimulation.** (A) Geometries used in the simulations were the “5nodes” geometries (Fig 1A). Boundary conditions were absorbing at the extremity of node 5 (blue), while the remaining boundaries were reflective (green). This mimics the connection of the modeled astrocyte branchlet to the rest of the cell. (B) (Top) Neuronal stimulation protocol simulated for each geometry: node 1 was stimulated at  $t=t_0=1\text{s}$  ( $k_{Ca}=0\text{ s}^{-1}$ ), while  $\text{Ca}^{2+}$  activity was monitored in nodes 1 and 2. (Bottom) Representative [Ca-GCaMP] traces in nodes 1 and 2, expressed as SNR (see Methods), for  $d_{\text{shaft}}=d_0$  (red),  $\frac{d_0}{2}$  (black) and  $\frac{d_0}{3}$  (blue). (C1)  $\text{Ca}^{2+}$  peak probability increases when  $d_{\text{shaft}}$  decreases in nodes 1 (\*\*\*) and 2 (\*\*). (C2) Time to 1<sup>st</sup> peak does not change with  $d_{\text{shaft}}$ , both in node 1 (p-value=0.85) and 2 (p-value=0.90). (C3) Peak amplitude increases when  $d_{\text{shaft}}$  decreases in nodes 1 (p-value=0.0056 \*\*) and 2 (p-value=0.0021 \*\*). (C4) Peak duration increases when  $d_{\text{shaft}}$  decreases in nodes 1 (p-value=0.0051 \*\*) and 2 (p-value=0.014 \*). (C5) The frequency of IP<sub>3</sub>R opening increases when  $d_{\text{shaft}}$  decreases in both nodes 1 and 2 (\*\*). Note that there were no  $\text{Ca}^{2+}$  peak in simulations with  $d_{\text{shaft}}=d_0$ .  $\text{Ca}^{2+}$  peak characteristics were not statistically different between node 1 and 2. Data are represented as mean  $\pm$  STD, n=20 for each geometry. The effect of  $d_{\text{shaft}}$  on each  $\text{Ca}^{2+}$  signal characteristic was tested using one-way ANOVA. Significance is assigned by \* for  $p \leq 0.05$ , \*\* for  $p \leq 0.01$ , \*\*\* for  $p \leq 0.001$ .

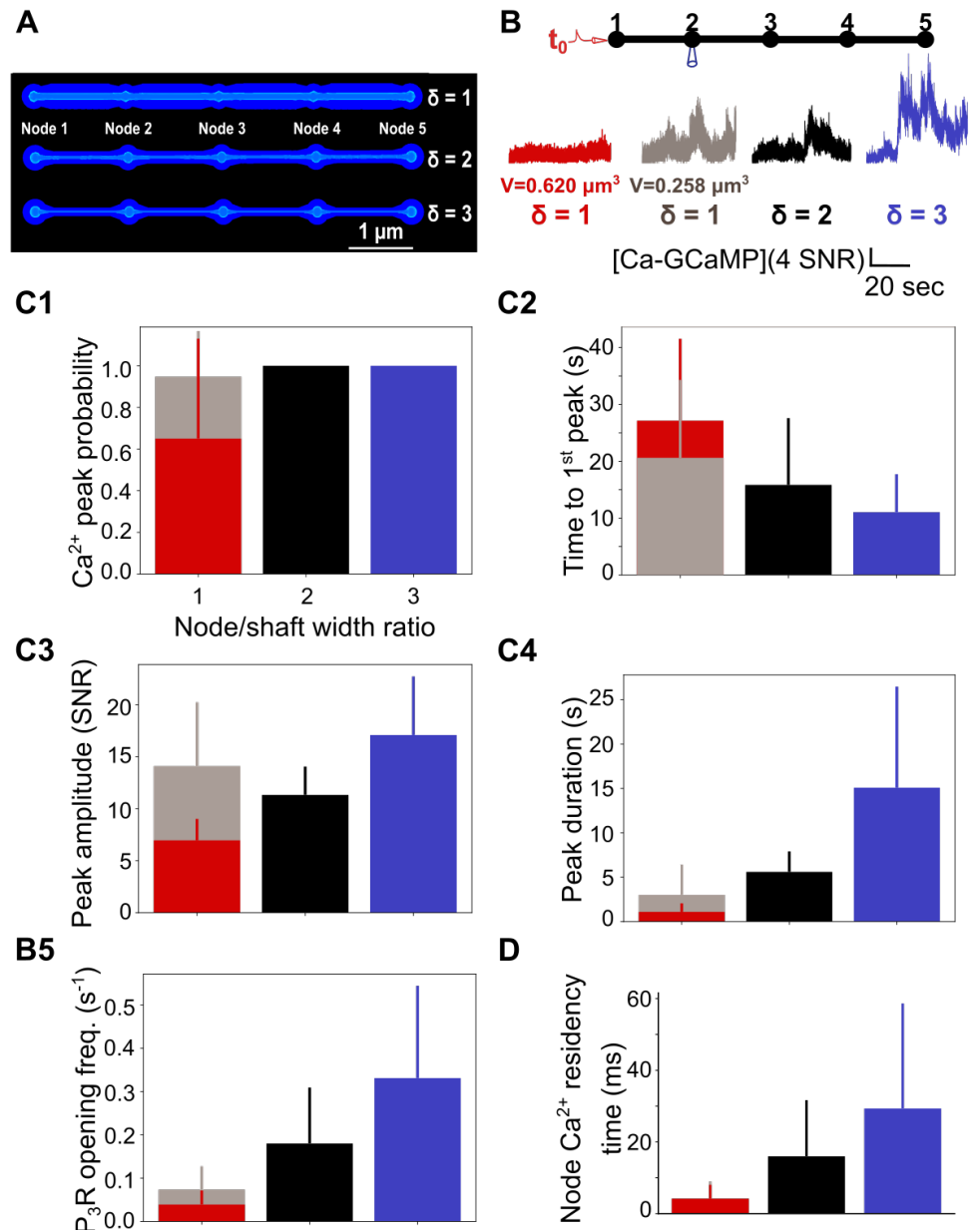
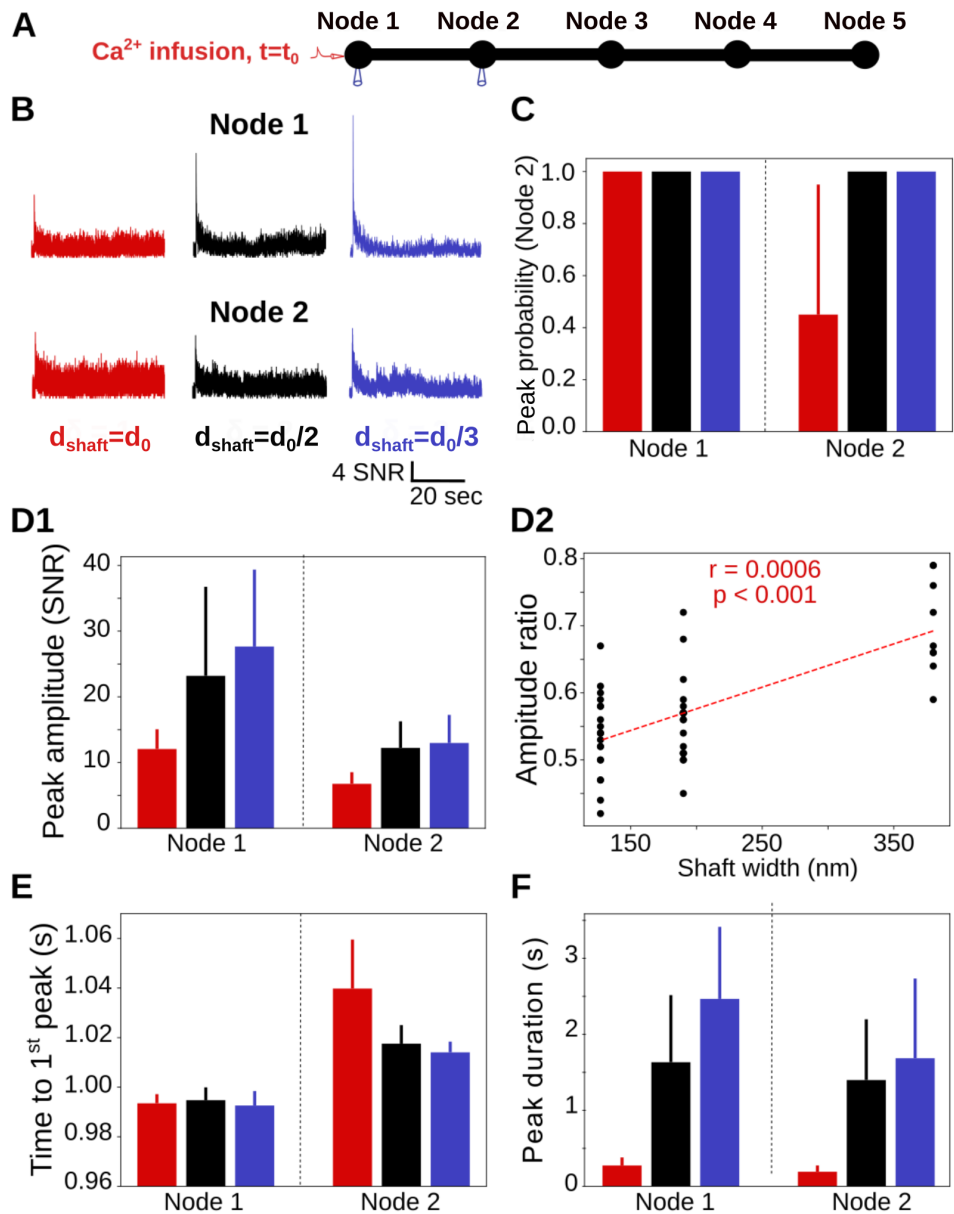
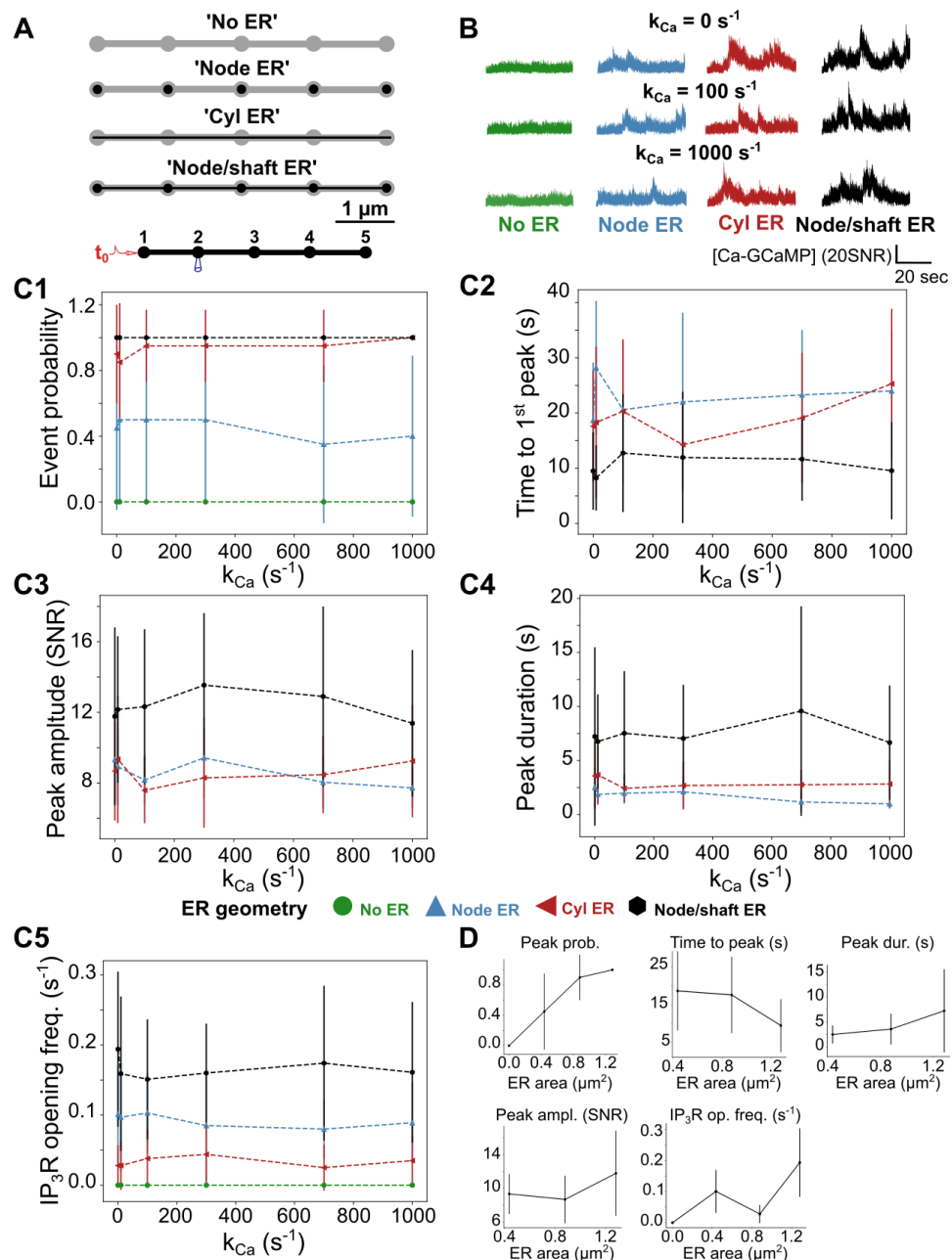


**Figure 3-Figure supplement 4. Node/shaft width ratio and node volume control local  $\text{Ca}^{2+}$  activity.** (A) Screenshots from STEPS visualization toolkit revealing meshes used in this study, that contain 5 identical nodes and 4 identical shafts. (B) (Top) Neuronal stimulation protocol simulated for each geometry: node 1 was stimulated at  $t=t_0=1\text{s}$  ( $k_{Ca}=0\text{ s}^{-1}$ ), while  $\text{Ca}^{2+}$  activity was recorded in node 2. (Bottom) Representative  $\text{Ca}^{2+}$  traces in node 2 in geometries with node/shaft width ratio  $\delta = \frac{d_0}{d_{shaft}}$  = 1 (red and gray), 2 (black) and 3 (blue), expressed as SNR (see Methods). Red and gray traces correspond to  $\text{Ca}^{2+}$  signals in geometries with  $\delta=1$  and a volume  $V_1=0.620\ \mu\text{m}^3$  and  $V_1=0.258\ \mu\text{m}^3$ , respectively. Black and blue traces were recorded in geometries with  $V_2=0.263\ \mu\text{m}^3$  and  $V_3=0.195\ \mu\text{m}^3$ , respectively. (C) Quantification of  $\text{Ca}^{2+}$  signal characteristics depending on node/shaft width ratio  $\delta$  and on process volume. Data are represented as mean  $\pm$  STD,  $n=20$  for each geometry. (C1)  $\text{Ca}^{2+}$  peak probability does not vary with  $\delta$  when  $V_1=0.258\ \mu\text{m}^3$  (p-value=0.22). (C2) Time to 1<sup>st</sup> peak decreases with  $\delta$  (p-value=0.0018 \*). (C3) Peak amplitude does not vary with  $\delta$  when  $V_1=0.258\ \mu\text{m}^3$  (p-value=0.16). (C4) Peak duration increases with  $\delta$ , for both  $V_1=0.620\ \mu\text{m}^3$  and  $V_1=0.258\ \mu\text{m}^3$  (\*\*\*). (C5) The frequency of  $\text{IP}_3\text{R}$  opening increases with  $\delta$ , for both  $V_1=0.620\ \mu\text{m}^3$  and  $V_1=0.258\ \mu\text{m}^3$  (\*\*\*). (D)  $\text{Ca}^{2+}$  residency time in nodes increases with  $\delta$ , for both  $V_1=0.620\ \mu\text{m}^3$  and  $V_1=0.258\ \mu\text{m}^3$  (\*\*\*,  $n=300$ ). The effect of node/shaft width ratio on each  $\text{Ca}^{2+}$  signal characteristic was tested using one-way ANOVA. Significance is assigned by \* for  $p \leq 0.05$ , \*\* for  $p \leq 0.01$ , \*\*\* for  $p \leq 0.001$ .



752

**Figure 3-Figure supplement 5. Thin shafts enhance local spontaneous Ca<sup>2+</sup> activity.** (A) Neuronal stimulation protocol simulated for each geometry. 200 Ca<sup>2+</sup> ions were infused in Node 1 at time t=t<sub>0</sub>, while Ca<sup>2+</sup> activity was recorded in nodes 1 and 2. (B) Representative Ca<sup>2+</sup> traces in node 1 (top) and node 2 (bottom) for  $d_{\text{shaft}}=d_0$  (red),  $\frac{d_0}{2}$  (black) and  $\frac{d_0}{3}$  (blue), expressed as SNR (see Methods). (C) Ca<sup>2+</sup> peak probability increases when  $d_{\text{shaft}}$  decreases in node 2 (\*\*\*). Note that peak probability is 1 in node 1 as the injection of 200 Ca<sup>2+</sup> ions in node 1 results in a local Ca-GCaMP peak for all seed values tested. (D1) Peak amplitude increases when  $d_{\text{shaft}}$  decreases in node 1 (\*\*\*) and 2 (\*\*\*). (D2) The ratio between peak amplitude in node 2 and in Node 1 increases with shaft width (Spearman  $r=0.0006$ , p-value < 0.001 \*\*\*). (E) Time to 1<sup>st</sup> peak in node 2 increases with  $d_{\text{shaft}}$  (\*\*\*). Note that time to 1<sup>st</sup> peak does not vary with  $d_{\text{shaft}}$  in node 1 as it occurs quickly after Ca<sup>2+</sup> injection, through the binding of the injected Ca<sup>2+</sup> ions to GCaMP molecules. (F) Peak duration increases when  $d_{\text{shaft}}$  decreases in node 1 (\*\*\*) and 2 (\*\*\*). Note that Ca<sup>2+</sup> peak characteristics were not statistically different between nodes 1 and 2. Data are represented as mean ± STD, n=20 for each geometry. The effect of  $d_{\text{shaft}}$  on each Ca<sup>2+</sup> signal characteristic was tested using one-way ANOVA. Significance is assigned by \* for  $p \leq 0.05$ , \*\* for  $p \leq 0.01$ , \*\*\* for  $p \leq 0.001$ .



753

**Figure 3-Figure supplement 6.  $\text{Ca}^{2+}$  peak probability, amplitude and duration decrease with ER surface area.** (A) As the shape and distribution of the ER in fine processes have not been characterized in live tissue so far but are likely highly variable (Aboufaires El Alaoui et al., 2021), simulations were performed in meshes with various ER shapes: "No ER", "Node ER" and "Node/shaft ER", in which there was no ER, discontinuous ER in nodes or an ER consisting in node/shaft alternations, respectively. (B) (Top) Neuronal stimulation protocol simulated for each geometry: node 1 was stimulated at  $t=t_0=1\text{s}$ , while  $\text{Ca}^{2+}$  activity was monitored in nodes 1 and 2. (Bottom) Representative  $\text{Ca}^{2+}$  traces in node 2, in "No ER" (green), "Node ER" (blue) and "Node/shaft ER" (black) geometries  $d_{\text{shaft}} = \frac{d_0}{2}$ , for  $k_{Ca} = 0, 10, 100, 300, 700$  and  $1000 \text{ s}^{-1}$ , expressed as SNR (see Methods). (C) Quantification of peak characteristics depending on ER geometry and  $k_{Ca}$ .  $\text{Ca}^{2+}$  peak probability (\*\*\*, C1), time to 1<sup>st</sup> peak (\*\*\*, C2), peak amplitude (\*\*\*, C3), duration (\*\*\*, C4) and the frequency of IP<sub>3</sub>R opening (\*\*\*, C5) vary with the ER morphology. Note that  $\text{Ca}^{2+}$  peak characteristics did not vary with  $k_{Ca}$ . (D) Time to 1<sup>st</sup> decreases as ER surface area increases (\*\*\*), while  $\text{Ca}^{2+}$  peak probability (\*\*\*), amplitude (\*\*\*), and duration (\*\*\*), as well as the frequency of IP<sub>3</sub>R opening (\*\*\*), increase as ER surface area increases,  $k_{Ca} = 0 \text{ s}^{-1}$ . Data are represented as mean  $\pm$  STD,  $n=20$  for each geometry. Significance is assigned by \* for  $p \leq 0.05$ , \*\* for  $p \leq 0.01$ , \*\*\* for  $p \leq 0.001$ .

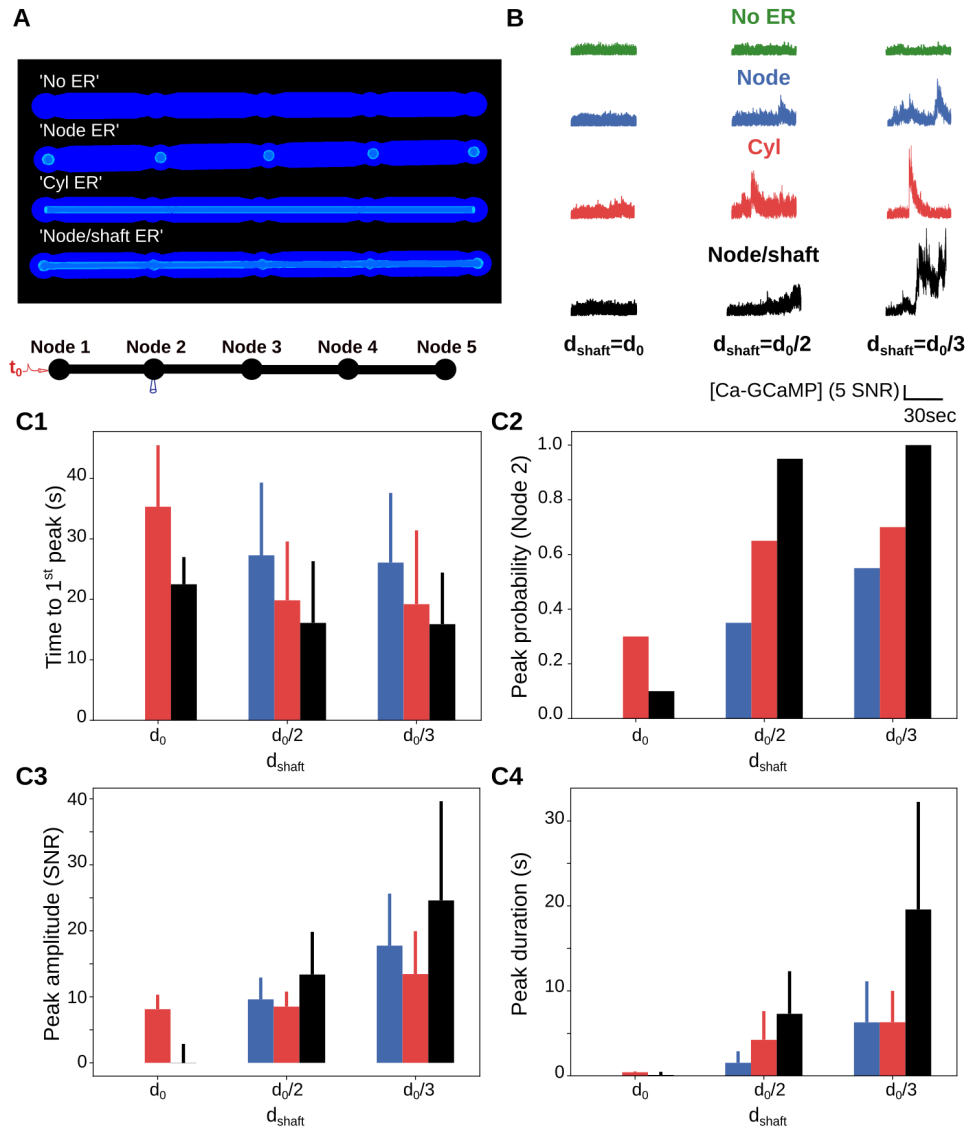


**Figure 3-Figure supplement 7. Local  $\text{Ca}^{2+}$  activity increases when shaft diameter decreases, for all ER geometries tested.** (A) Screenshots displaying the geometries used to investigate the effect of ER geometry on  $\text{Ca}^{2+}$  dynamics: "No ER", "Node ER", "Node/shaft ER" and "Cyl ER". (B) (Top) Neuronal stimulation protocol simulated for each geometry: node 1 was stimulated at  $t=t_0=1s$  ( $k_{\text{Ca}}=0 s^{-1}$ ), while  $\text{Ca}^{2+}$  activity was monitored in node 2. (Bottom) Representative  $\text{Ca}^{2+}$  traces in node 2 for  $d_{\text{shaft}}=d_0$  (left),  $\frac{d_0}{2}$  (center) and  $\frac{d_0}{3}$  (right), in "No ER" (green), "Node ER" (blue), "Cyl ER" (red) and "Node/shaft ER" (black) geometries, expressed as SNR (see Methods). (C) Quantification of the effect of  $d_{\text{shaft}}$  on  $\text{Ca}^{2+}$  dynamics. Note that no bar is visible for simulations in "Node ER"  $d_{\text{shaft}}=d_0$  geometries as no peak was detected. Results in "Node/shaft ER" geometries are presented in Fig3 but are added here (black bars) for comparison. (C1) Time to 1<sup>st</sup> peak in node 2 does not vary with  $d_{\text{shaft}}$  in "Node ER" simulations (p-value=0.85) but increases with  $d_{\text{shaft}}$  in "Cyl ER" simulations (p-value= 0.021 \*). (C2)  $\text{Ca}^{2+}$  peak probability in node 2 increases when  $d_{\text{shaft}}$  decreases in "Node ER" simulations (\*\*\*) and in "Cyl ER" simulations (p-value=0.01 \*). (C3) Peak amplitude increases when  $d_{\text{shaft}}$  decreases in "Node ER" geometries (p-value=0.027 \*) and in "Cyl ER" (p-value=0.01 \*). (C4) Peak duration increases when  $d_{\text{shaft}}$  decreases in "Node ER" simulations (p-value=0.028 \*) and in "Cyl ER" simulations (p-value=0.001 \*\*). Data are represented as mean  $\pm$  STD, n=20, for each geometry. The effect of  $d_{\text{shaft}}$  on each  $\text{Ca}^{2+}$  signal characteristic was tested using one-way ANOVA. Significance is assigned by \* for  $p \leq 0.05$ , \*\* for  $p \leq 0.01$ , \*\*\* for  $p \leq 0.001$ .

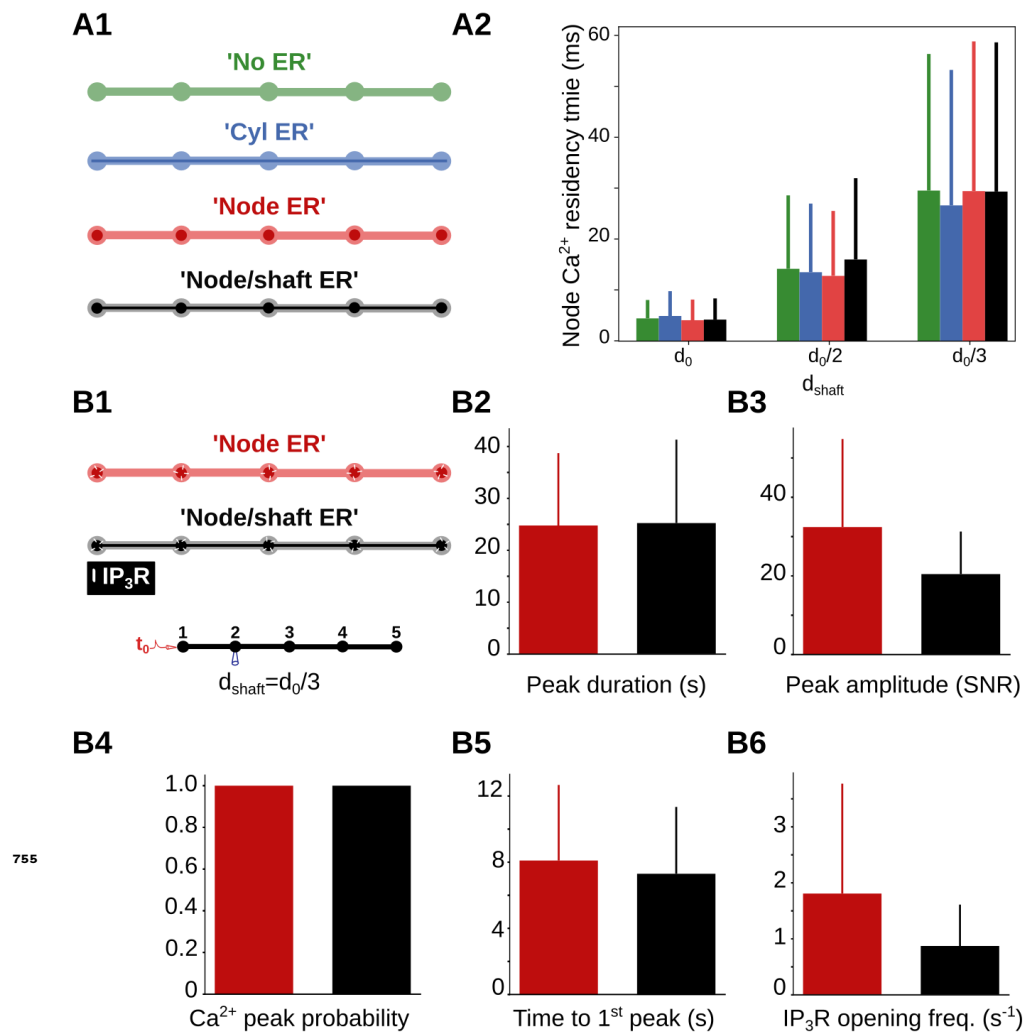


**Figure 3-Figure supplement 8. Sensitivity study of the effect of ER morphology on  $\text{Ca}^{2+}$  dynamics.** (A) Node  $\text{Ca}^{2+}$  residency time is not influenced by ER morphology. (A1) One  $\text{Ca}^{2+}$  ion was added in node 1 in geometries with different ER shapes: "No ER" (green), "Node ER" (blue), "Cyl ER" (red) and "Node/shaft ER" (black). (A2) For all ER shapes tested,  $\text{Ca}^{2+}$  residency time in nodes increases when  $d_{\text{shaft}}$  decreases. Node  $\text{Ca}^{2+}$  residency time does not change depending on ER morphology, suggesting that cellular morphology has a greater influence on compartmentalization than ER morphology in the meshes used in this study. Data are represented as mean  $\leq$  STD,  $n=300$  for each geometry. (B) Sensitivity study of the effect of ER morphology on  $\text{Ca}^{2+}$  dynamics with constant number of  $\text{IP}_3\text{R}$ s. (B1) Simulations were performed in 'Node ER' (red) and "Node/shaft ER" (black) geometries with  $\text{IP}_3\text{R}$  channels (white) located in nodes (Top), resulting in a constant number of  $\text{IP}_3\text{R}$  channels for both ER shapes. Node 1 was stimulated at  $t=t_0=1\text{ s}$  ( $k_{\text{Ca}}=0\text{ s}^{-1}$ ), while  $\text{Ca}^{2+}$  activity was monitored in node 2 (bottom). (B2-6) Quantification of  $\text{Ca}^{2+}$  signals depending on ER morphology with constant number of  $\text{IP}_3\text{R}$  in node 2,  $d_{\text{shaft}} = \frac{d_0}{3}$ . Data are represented as mean  $\leq$  STD,  $n=20$  for each geometry.  $\text{Ca}^{2+}$  peak duration (B2), amplitude (B3), probability (B4) and delay (B5) do not vary with ER morphology when  $\text{IP}_3\text{R}$  channels are located in nodes. (B6)  $\text{IP}_3\text{R}$  opening frequency does not significantly differ between "Node ER" and "Node/shaft ER" geometries ( $p\text{-value}=0.06$ ). Those results suggest that the decreased  $\text{Ca}^{2+}$  activity in branchlets that contain discontinuous ER reported in Fig 4 mainly results from the decreased number of  $\text{IP}_3\text{R}$  channels associated with the decreased ER surface area of "Node ER" compared to "Node/shaft ER" morphology.

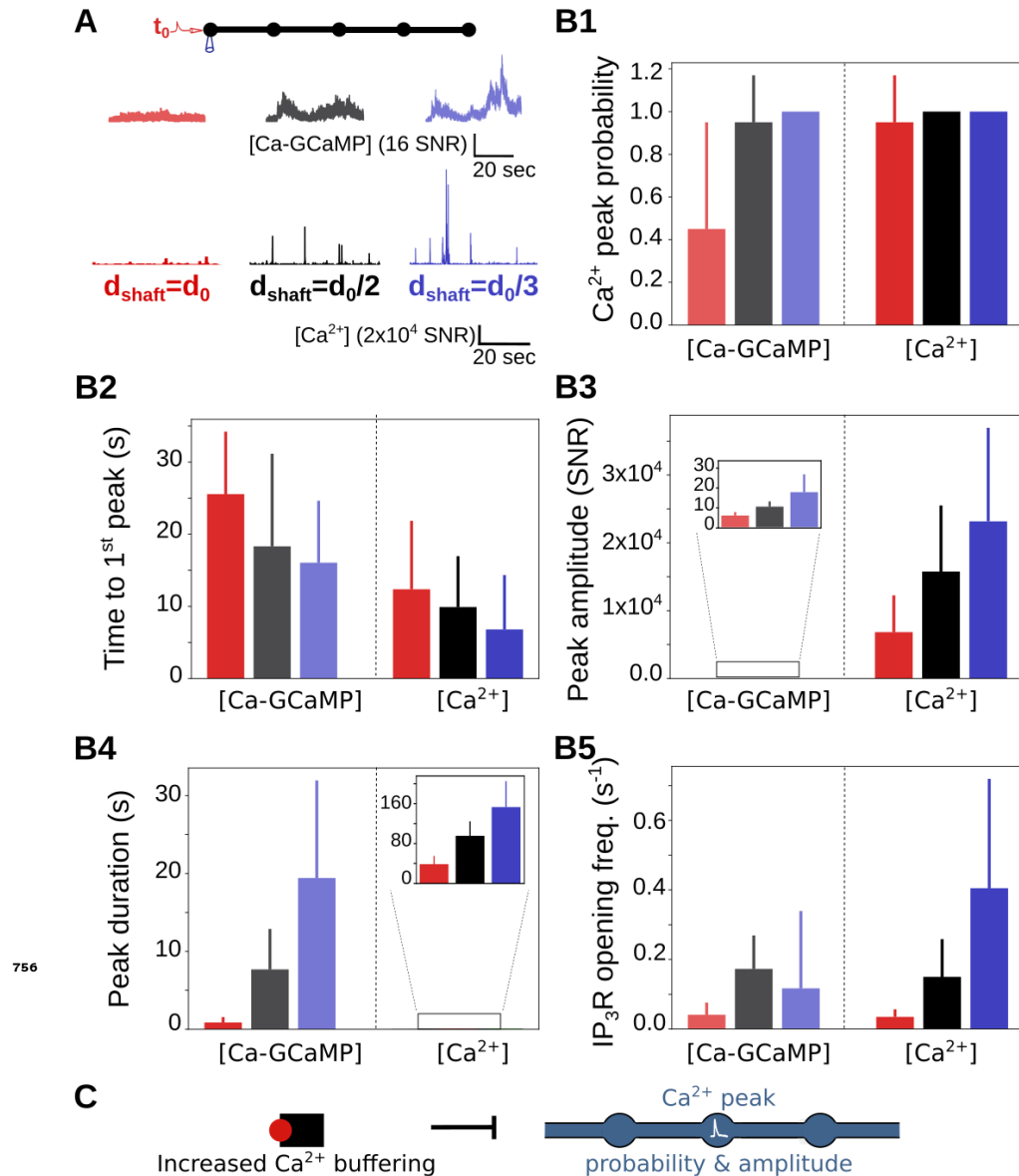


**Figure 3—Figure supplement 9. Ca<sup>2+</sup> indicators alter Ca<sup>2+</sup> peak characteristics.** (A) In order to investigate free Ca<sup>2+</sup> peak probability, no GCaMP molecules were added to the model. (Top) At  $t=t_0=1s$ , node 1 was stimulated ( $k_{Ca}=0 s^{-1}$ ), while Ca<sup>2+</sup> concentration was monitored in node 1. The geometry used for  $d_{\text{shaft}}=d_0$  corresponds to the geometry presented in Fig 1A. (Middle) Representative Ca-GCaMP traces in node 1, in simulations containing GCaMP molecules in geometries with shaft width  $d_{\text{shaft}} = d_0$  (light red),  $\frac{d_0}{2}$  (grey) and  $\frac{d_0}{3}$  (light blue). (Bottom) Representative free Ca<sup>2+</sup> traces in node 1, in the absence of GCaMP molecules, in geometries with shaft width  $d_{\text{shaft}} = d_0$  (red),  $\frac{d_0}{2}$  (black) and  $\frac{d_0}{3}$  (blue). The amplitude of Ca-GCaMP and free Ca<sup>2+</sup> signals is expressed as SNR (see Methods). (B) Characteristics of free Ca<sup>2+</sup> signals depending on  $d_{\text{shaft}}$ . Ca-GCaMP signals measured in simulations from Fig 3 are presented for comparison. (B1) Free Ca<sup>2+</sup> peak probability does not vary with  $d_{\text{shaft}}$  (p-value=0.22). Ca-GCaMP peak probability is lower than free Ca<sup>2+</sup> peak probability for  $d_{\text{shaft}}=d_0$  (\*\*\*). (B2) Time to 1<sup>st</sup> free Ca<sup>2+</sup> peak increases with  $d_{\text{shaft}}$  (\*\*\*). Time to 1<sup>st</sup> Ca-GCaMP peak is higher than time to 1<sup>st</sup> free Ca<sup>2+</sup> peak, for any value of  $d_{\text{shaft}}$  (\*\*\*). (B3) Free Ca<sup>2+</sup> peak amplitude increases when  $d_{\text{shaft}}$  decreases (\*\*\*). Ca-GCaMP peak amplitude is lower than free Ca<sup>2+</sup> peak amplitude, for any value of  $d_{\text{shaft}}$  (\*\*\*). (B4) Free Ca<sup>2+</sup> peak duration increases when  $d_{\text{shaft}}$  decreases (\*\*\*). Ca-GCaMP peak duration is higher than free Ca<sup>2+</sup> peak duration, for any value of  $d_{\text{shaft}}$  (\*\*\*). (B5) The frequency of IP<sub>3</sub>R opening increases when  $d_{\text{shaft}}$  decreases (\*\*\*). (C) Schematic summarizing the main result from this figure: increased Ca<sup>2+</sup> buffering is associated with decreased Ca<sup>2+</sup> peak probability and amplitude. Data are represented as mean  $\pm$  STD, n=20 for each geometry. The effect of  $d_{\text{shaft}}$  on each free Ca<sup>2+</sup> signal characteristic was tested using one-way ANOVA. Significance is assigned by \* for  $p \leq 0.05$ , \*\* for  $p \leq 0.01$ , \*\*\* for  $p \leq 0.001$ .

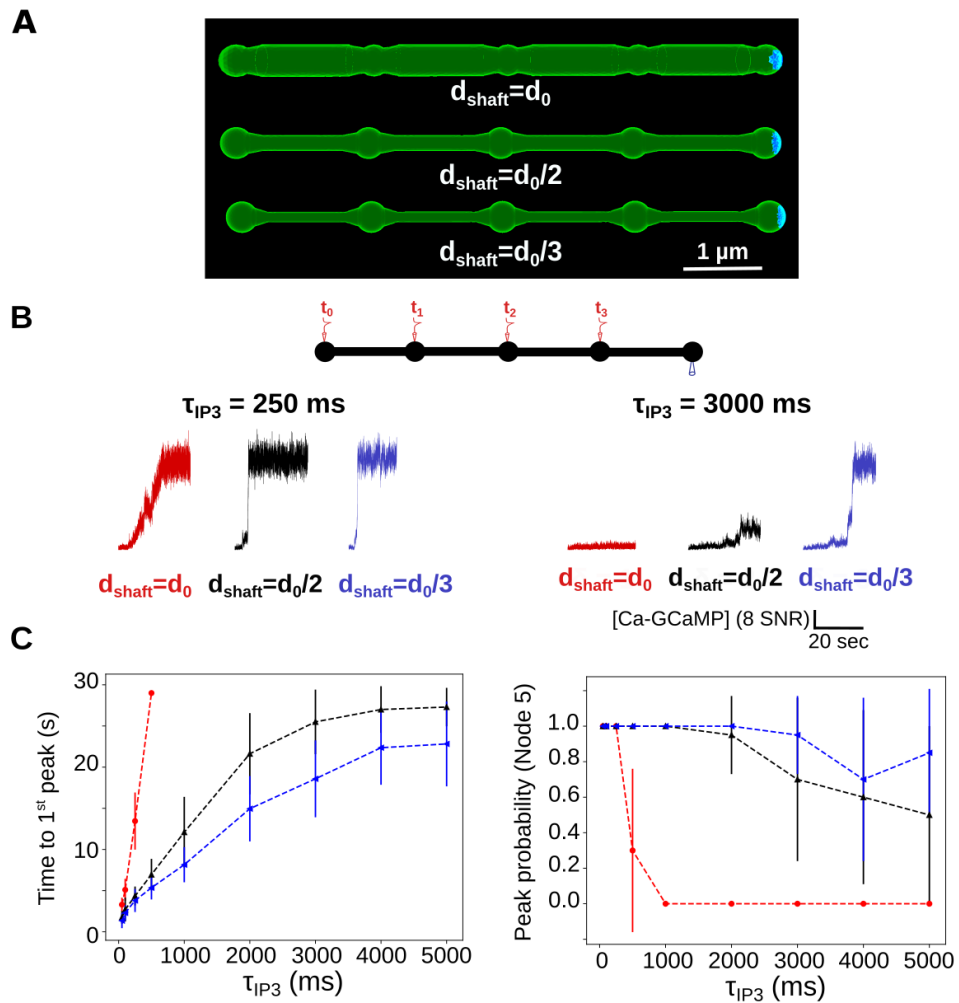


**Figure 5-Figure supplement 1. Sensitivity study of the effect of boundary conditions on local  $\text{Ca}^{2+}$  activity upon repeated neuronal stimuli.** (A) Simulations were performed in the “5nodes” geometries (Fig1). Boundary conditions were absorbing at the extremity of node 5 (blue) while the remaining boundaries were characterized by reflective boundary conditions (green). Those boundary conditions mimic the connection of the modeled astrocyte branchlet to the rest of the cell. (B) (Top) node 1 was stimulated at  $t=t_0=5s$ , node 2 at  $t_0 + \tau_{IP3}$ , node 3 at  $t_0 + 2\tau_{IP3}$  and node 4 at  $t_0 + 3\tau_{IP3}$ ,  $k_{Ca}=0 s^{-1}$ , while  $\text{Ca}^{2+}$  activity was monitored in node 5. (Bottom) Representative  $\text{Ca}^{2+}$  traces for  $d_{\text{shaft}}=d_0$  (red),  $\frac{d_0}{2}$  (black) and  $\frac{d_0}{3}$  (blue), with  $\tau_{IP3}=250\text{ms}$  (left) and  $3000\text{ms}$  (right), expressed as SNR (see Methods). (C) (Left) Time to 1<sup>st</sup> peak in node 5 increases with  $\tau_{IP3}$  for  $d_{\text{shaft}}=d_0$  (\*\*\*) ,  $d_{\text{shaft}}=\frac{d_0}{2}$  (\*\*\*) and  $d_{\text{shaft}}=\frac{d_0}{3}$  (\*\*\*) . Time to 1<sup>st</sup> peak is higher for  $d_{\text{shaft}}=d_0$  compared to  $d_{\text{shaft}}=\frac{d_0}{2}$  and  $d_{\text{shaft}}=\frac{d_0}{3}$ . (Right)  $\text{Ca}^{2+}$  peak probability in node 5 is lower for  $d_{\text{shaft}}=d_0$  compared to  $d_{\text{shaft}}=\frac{d_0}{2}$  and  $d_{\text{shaft}}=\frac{d_0}{3}$  and decreases as  $\tau_{IP3}$  increases for  $d_{\text{shaft}}=d_0$  (\*\*\*) and  $d_{\text{shaft}}=\frac{d_0}{2}$  (\*\*\*) but not  $d_{\text{shaft}}=\frac{d_0}{3}$  (p-value=0.054). Note that  $\text{Ca}^{2+}$  peak probability was lower and time to 1<sup>st</sup> peak higher compared to simulations with reflective boundary conditions. Data are represented as mean  $\pm$  STD,  $n=20$  for each value of  $d_{\text{shaft}}$  and of  $\tau_{IP3}$ . Lines are guides for the eyes. The effect of  $d_{\text{shaft}}$  on each  $\text{Ca}^{2+}$  signal characteristic was tested using one-way ANOVA. Significance is assigned by \* for  $p \leq 0.05$ , \*\* for  $p \leq 0.01$ , \*\*\* for  $p \leq 0.001$ .